Politecnico di Torino

Politecnico di Torino

Master's Degree in Nanotechnologies for ICTs

Lab-On-a-Chip development for barrier model monitoring

Supervisors:
Prof. Matteo Cocuzza
PhD Simone Luigi Marasso
PhD Alberto Ballesio
MSc Jovana Babić

Candidate:
Lucrezia Regalzi

A.y. 2024/2025
Graduation session: November/December 2025

Abstract

In the context of D^3 4 HEALTH Foundation research on digital health technologies, this work contributes to the development of innovative tools for biomedical applications, with potential impact on diagnosis, monitoring and treatment. The aim of this thesis is to optimize a multi-layer microfluidic platform for cell culture and analysis, with the integration of Organic Electrochemical Transistors (OECTs) for real-time monitoring of cellular responses. Starting from a previously developed microfluidic device, the design was modified to enable the culture of a human skin cell model and the incorporation of OECT sensors. The methodology involved the CAD design of the microfluidic platform composed of three different layers: two for cell culture and microfluidic connections, with a central chamber aimed at hosting the barrier model on a porous membrane, and the third one for bottom sealing of the chamber and OECTs integration. Two versions of the device were developed to embed two different membranes to be evaluated, a (38 ± 3) µm thick Polycarbonate (PC) one by Oxyphen and a (210 ± 10) µm thick silk one produced by KLISBio. The manufacturing process involved soft lithography, with the 3D-printing of master molds for the different layers and then the replica molding in PDMS. The final assembly of the multi-layer platform was performed through two techniques to be compared: adhesive bonding with a thin film of PDMS and plasma bonding. The OECTs were fabricated in clean room environment and then completed with the inkjet deposition of PEDOT:PSS, which constitutes the channel material. The OECT chips were complemented by gold gates produced in clean room, which are biocompatible and can be functionalized to enable biosensing.

The developed Lab-on-a-Chip (LOC) devices were subjected to microfluidic leakage tests, achieving successful results with the commercial membrane and plasma bonding technique. The silk membrane version requires further optimization to improve the flow and avoid the bending of the membrane to allow hosting the skin model. The integration of OECTs in the multi-layer platform was successfully achieved, with the devices demonstrating stable electrical characteristics and sensitivity to ionic solutions. The future work will involve the seeding of human skin cells on the membranes, the functionalization of OECT gates for specific biomarker detection and the real-time monitoring of cellular responses under various conditions.

Aknowledgements

Nell'ambito del mio progetto di tesi ho avuto la fortuna di lavorare al fianco di Jovana, che mi ha guidata e supportata anche a distanza e a cui devo molto per la pazienza e la disponibilità che ha sempre dimostrato. Un sincero ringraziamento va anche alle altre dottorande e ai dottorandi del gruppo, che mi hanno accolta da subito ed aiutata in diverse occasioni.

Con questo passo giunge al termine un percorso di studi che ha richiesto impegno, dedizione e costanza, ma che mi ha anche regalato molte soddisfazioni. Con il raggiungimento di questo traguardo voglio esprimere la mia gratitudine alla mia famiglia, per il costante supporto, e ai miei amici, per aver condiviso con me momenti di fatica e di leggerezza. Gli anni universitari non sarebbero stati gli stessi senza di voi.

Contents

List of Figures

List of Tables

List of Acronyms and Symbols

Acronyms

$D^3$4HEALTH	Digital Driven Diagnostics, Prognostics and Therapeutics for Sustainable Health Care
PNRR	Piano Nazionale di Ripresa e Resilienza (Italian National Recovery and Resilience Plan)
PNC	Piano Nazionale Complementare (Italian National Complementary Plan)
LOC	Lab-on-a-Chip
PoC	Point-of-Care
OoC	Organ-on-a-Chip
OECT	Organic Electrochemical Transistor
DNA	Deoxyribonucleic Acid
PDMS	Polydimethylsiloxane
GelMa	Gelatin Methacryloyl
IL-17	Interleukin 17
TNF-α	Tumor Necrosis Factor-alpha
PMMA	Poly(methyl methacrylate)
OTFT	Organic Thin-Film Transistor
OFET	Organic Field-Effect Transistor
EGOT	Electrolyte-Gated Organic Transistor
FET	Field Effect Transistor
EGOFET	Electrolyte-Gated Organic Field Effect Transistor
MOSFET	Metal Oxide Semiconductor Field Effect Transistor
OMIEC	Organic Mixed Ionic-Electronic Conductor
PEDOT	Poly(3,4-ethylenedioxythiophene)
PSS	Polystyrene sulfonate
PEDOT:PSS	Poly(3,4-ethylenedioxythiophene) polystyrene sulfonate
OSC	Organic Semiconductor
OMIEC	Organic Mixed Ionic-Electronic Conductor
CP	Conjugated Polymer
DOS	Density of States
HOMO	Highest Occupied Molecular Orbital
LUMO	Lowest Unoccupied Molecular Orbital
DiSAT	"Dipartimento di Scienza Applicata e Tecnologia"
INRiM	"Istituto Nazionale di Ricerca Metrologica"
PiQuET	"Piemonte Quantum Enabling Technology"
CAD	Computer Aided Design
PC	Polycarbonate

UV	Ultraviolet
SMU	Source/Measure Unit
DOD	Drop on Demand
DBSA	Dodecylbenzenesulfonic Acid
GOPS	(3-Glycidyloxypropyl)trimethoxysilane
SAM	Self-Assembled Monolayer
3-MPA	3-Mercaptopropionic Acid
MES	2-(N-morpholino)ethanesulfonic acid
EDC	1-ethyl-3-(3-dimethylaminopropyl)carbodiimide
NHS	N-hydroxysuccinimide
Sulfo-NHS	N-hydroxysulfosuccinimide
Ang2	Angiopoietin-2
anti-Ang2	Angiopoietin-2 antibody
PBS	Phosphate Buffered Saline
CC BY	Creative Commons Attribution

Symbols

V_{DS}	Drain-Source Voltage (V)
V_{GS}	Gate-Source Voltage (V)
V_{th}	Threshold Voltage (V)
$V_{DS,sat}$	Drain-Source Saturation Voltage (V)
μ_p	Charge Carrier (Holes) Mobility ($cm^2\ V^{-1}\ s^{-1}$)
C_{ox}	Gate Oxide Capacitance per unit area ($F\ cm^{-2}$)
W	Channel Width (cm)
L	Channel Length (cm)
λ	Channel-Length Modulation Parameter (V^{-1})
I_D	Drain Current (A)
I_G	Gate Current (A)
V_G	Gate Voltage (V)
I_{ON}	ON (Drain) Current (A)
I_{OFF}	OFF (Drain) Current (A)
g_m	Transconductance (S)
V_{th}	Threshold Voltage (V)

Introduction

With the continuous evolution of engineering and digital technologies, the healthcare sector is one of the most important fields that can benefit from the progress made in these areas. The *Digital Driven Diagnostics, Prognostics and Therapeutics for Sustainable Health Care* ($D^3$4HEALTH) *Foundation*[20] promotes the development of innovative solutions that integrate engineering methods with clinical needs, aiming at improving diagnosis, monitoring and treatment of diseases. Politecnico di Torino is a partner in the $D^3$4HEALTH project, as part of the research activities funded by the Italian National Recovery and Resilience Plan (PNRR) in the context of Complementary National Plan (PNC) for Health[20;21].

Among the areas addressed by these initiatives, skin research stands out for its complexity and relevance in healthcare. Skin, the largest organ of the human body, plays a key role as a barrier, as it is in direct contact with the external environment, thus interacting with a variety of chemical, physical and biological agents. Having a skin model to study can be crucial for different purposes, from testing products to understanding the behaviour of the cells under specific conditions. A typical application regards the analysis of the permeation of drugs and cosmetics to assess their effectiveness and safety[22]. Moreover, the problem of antibiotic resistance is becoming more and more relevant nowadays, thus having tools to study drug effectiveness on specific bacteria is fundamental to develop appropriate therapies[23]. These kinds of experiments prior to human trials were historically performed on animal models, with sources dated back to Ancient Greece and Rome[22]. In more recent times, animal testing has been restricted not only due to ethical concerns, but also because of limitations in predicting human responses. The first alternative approach was represented by 2D cell cultures, which however cannot replicate the complex architecture of human tissues. Therefore, the development of 3D *in vitro* skin models has gained significant attention in the last century, as they can better mimic the physiological and structural characteristics of human skin, providing more reliable results for testing and research purposes.[22;23;1]

In this framework, the development of technologies for *in vitro* models can contribute to the advancement of biomedical research from a close perspective, providing the platforms and tools necessary to study biological processes and test new therapies. Some of these technologies are generally referred to as Lab-on-a-chip (LOC) devices, platforms which integrate multiple laboratory functions on a single portable chip. The fabrication of these structures enables Point-of-Care (PoC) applications, allowing rapid and on-site analysis, with a small amount of reagents and samples. Microfluidics is the fundamental requirement for LOCs for handling small volumes of fluids. Working with microscopic distances has some advantageous consequences such as the rapid manipulation of the samples and therefore fast, high-throughput response, but also simply the achieved compactness of these devices, which makes

them portable and implies high parallelization, with the integration of multiple functions on a centimeter-sized apparatus. Microfluidics allows to precisely control the microenvironment inside the chip, making it suitable for cell culture applications. On this note, Organ-on-Chips (OoC) has arisen as a subcategory of LOCs, aiming to replicate the human physiology within the introduced microfluidic structures.[24;1]

Imran et al.[22] investigated and recapitulated the current state of the art of 3D *in vitro* skin models and some technologies used to develop them, such as organoids, microfluidics and OoC devices. Some OoC platforms for skin models are referenced in their work, in particular some microfluidic structures including one that allowed the culture of a two-layer tissue in an upper chamber, with nutrients supplied from a lower chamber. Licciardello et al.[25] developed a multi-layer microfluidic platform for the culture of a 3D model of alveolar tissue to study the alveolar-capillary barrier, enabling the co-culture of epithelial and endothelial cells. The proposed examples validate the microfluidic devices as promising tools to create an environment suitable for cell culture. A new frontier of these research include the integration of biosensors into the LOC apparatus, enabling the possibility of real-time monitoring of the cells conditions. Organic Electrochemical Transistors (OECTs) are emerging as effective biosensors for *in vitro* applications, due to their biocompatibility and stability in culture medium[26]. Lin et al.[26] collected various examples of OECTs used as biosensors for the detection of biomolecules, such as glucose, DNA and antibodies/antigens. The possibility to functionalize the gate electrode with specific receptors allows to target different analytes, making OECTs versatile devices for biosensing applications.

The motivation behind this work lies in the will to contribute to the engineering progress of innovative tools for biomedical research, addressing the growing need of reliable and ethically sustainable models that can replicate the complexity of human tissues. In this context, the main focus of this thesis is the development of a Lab-on-a-chip (LOC) platform for monitoring a skin barrier model. The platform is designed to host a 3D skin model, allowing the monitoring of its status through the electrical sensors with functionalized gold gates. Specific goals include the design and fabrication of a multi-layer PDMS (polydimethylsiloxane) microfluidic structure, the integration and characterization of OECT sensors, followed by the preliminary validation of the platform for cell culture applications, through microfluidic leakage tests and initial biosensing trials through gates functionalization.

The developed platform is intended to host a 3D *in vitro* skin model that closely mimics the architecture and function of human skin for testing therapeutic interventions. The 3D *in vitro* skin model to be used in the future perspective of this work is the one designed by Villata et al.[23] to replicate the structural and functional properties of human skin, providing a physiologically relevant platform for therapy testing. The model consists of two main compartments: a dermal layer composed of human fibroblasts embedded in a gelatin methacryloyl (GelMA) hydrogel and an epidermal layer formed by human keratinocytes cultured on top.[23] To introduce vascular components into the 3D skin model, endothelial cells together with supportive stromal cells would be included to form a pre-vascularized layer. In the original Transwell-based setup[23], these cells were placed on the lower surface of the membrane to promote interaction with the developing dermal compartment. For the microfluidic platform fabricated in this work, this strategy would be adapted by delivering and seeding the same cell populations through the chip channels, allowing them to at-

tach, organize and form vascular structures under dynamic flow conditions. The perfusion of culture medium through the channels would support cell viability and maturation until the dermal layer is added. In order to monitor the conditions of the skin model, OECT gates will be functionalized with specific receptors to detect relevant biomarkers, which selection can depend on factors such as specificity, sensitivity, cost feasibility, stability, rapid detection and reproducibility. Biomarkers are molecular indicators of biological processes, their detection can provide valuable information about the state of the skin model, such as inflammation or barrier integrity. The functionalization process involves modifying the surface of the gate electrodes with specific molecules that can selectively bind to the target biomarkers, enabling real-time monitoring of the skin model. Specific biomarkers can be used to monitor healthy skin by tracking epidermal differentiation markers (keratins 1/10, involucrin, loricrin, filaggrin), assessing lipid composition in the stratum corneum for barrier integrity and analyzing dermal proteins (collagens I/III/V, decorin) to ensure the extracellular matrix stability [27]. By selecting disease-related biomarkers, including inflammatory cytokines (IL-17, TNF-α), oxidative stress markers and genetic or molecular signatures associated with conditions such as psoriasis or atopic dermatitis, the platform could enable precise disease modeling and support personalized therapeutic strategies [28].

After this brief introduction, Chapter 1 provides an overlook of the theoretical background needed to understand the project, from the concept of LOC and OoC devices, to the working principles of OECTs and their applications as biosensors. Chapter 2 then explains the materials used in the work and the methods for the fabrication of platform and sensors, as well as for the successive tests. The obtained results regarding the fabrication, test and characterization of the platform and the OECTs are presented and discussed in Chapter 3. Finally, Chapter 4 summarizes the main findings of the thesis and suggests possible future developments.

Chapter 1

Theoretical Background

1.1 Lab-on-a-Chip

Lab-on-a-Chip (LOC) technology consists in the integration of different laboratory functions on a single chip of size from a few millimeters to a few square centimeters. As the name suggests, the basic idea behind these devices is to be able to perform laboratory analyses in a miniaturized format, making them portable, accessible and cost-effective. LOCs have a wide range of applications, including medical diagnostics, environmental monitoring, food safety, drug testing and development. The main advantages of such technology include the reduction of the volumes of reagents, going down to less than picoliters, the reduction of response times, the possibility of parallelization and automation of processes, and the portability of the devices, which allows for point-of-care (PoC) testing outside of traditional laboratory settings. A typical LOC device can be described as a microfluidic platform with the additional integration of biosensors, electronics and other components necessary for sample handling, analysis and detection, making this an interdisciplinary field of interest. Microfluidic elements are used to manipulate small volumes of fluids, allowing for precise control over the movement and mixing of samples and reagents. Biosensors integrated into the chip can detect specific biological or chemical analytes, providing real-time data on the sample being analyzed [24]. One of the principal sectors benefitting of LOC technology is biomedicine, since these devices can support mixing, analysis and detection of biological samples, even integrating electrical or optical measurements [29].

Different materials can be used for the construction of LOCs, including polymers (like PDMS, PMMA), glass and silicon, each offering specific advantages depending on the application requirements. Silicon can be considered one of the best known materials for microfabrication, allowing to achieve high resolution features and easy integration with electronic components. However, its high cost and fragility limit its use in disposable LOC devices. Glass is another popular material, with well established manufacturing technologies, which offers excellent optical properties, biocompatibility and chemical resistance, but it is also relatively expensive and fragile. Polymers, such as PDMS, are widely used due to their low cost, ease of fabrication and biocompatibility, making them ideal for biological applications. Their usual flexibility and transparency also make them suitable for optical detection methods commonly used in LOC applications. Polymeric chips can be manufactured using replication techniques, such as soft lithography, involving the creation of a master

used to mould the polymer into the desired structures.

1.1.1 Organ-on-Chip

Organ-on-Chip (OoC) technology represents an advanced subset of Lab-on-Chip (LOC) systems, specifically designed to replicate key physiological functions of the human body within a microfluidic platform. These devices typically consist of interconnected microchannels lined with living cells, organized to mimic the architecture and functionality of specific organs. By integrating mechanical forces, controlled fluid flow and biochemical gradients, OoC systems recreate dynamic physiological conditions, enabling the study of organ-level responses to drugs, toxins and pathological stimuli in a highly controlled environment.[1]

A distinctive feature of OoC platforms is their ability to incorporate real-time monitoring and imaging capabilities, allowing direct observation of cellular behavior, tissue responses and molecular interactions. This enables continuous observation and quantitative assessment of biological processes over time without interfering with the system integrity. Furthermore, OoC devices can be engineered in various configurations, ranging from single-organ models, ideal for focused investigations, to multi-organ systems that simulate inter-organ communication and systemic effects, thus offering a more complete representation of human physiology.[1;30]

The potential applications of OoC technology are many, meeting different domains and contributing to a new approach for studying and understanding biological systems as well as developing new therapeutic strategies. These platforms enable drug response studies, providing insights into pharmacokinetics and pharmacodynamics under physiologically relevant conditions. They support personalized medicine by allowing patient-specific cells to be integrated into the chip, customizing therapeutic strategies to individual genetic profiles. Additionally, OoC systems can constitute an important tool for the inspection of disease mechanisms, allowing to model complex pathologies such as cancer, neurodegenerative disorders and inflammatory diseases. Finally, they serve as powerful tools for drug screening and toxicity testing, reducing reliance on animal models and accelerating the drug discovery pipeline[1;31;32]. The different opportunities linked to OoC technology are summarized in Figure 1.1.

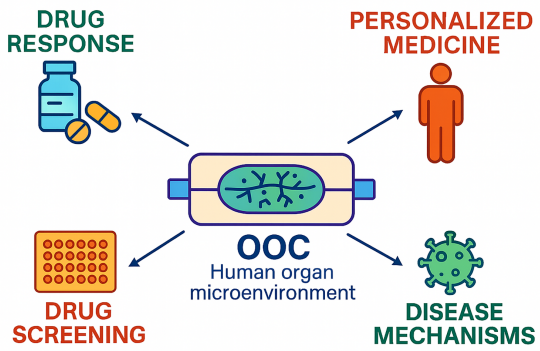

Figure 1.1: Illustration highlighting the diverse applications of OoC technology, including drug response studies, personalized medicine, disease mechanism exploration and drug screening. Adapted from Srivastava et al.[1].

1.1.2 Microfluidics for cell culture

The foundation of OoC technology lies in microfluidics, which allows for the precise manipulation of small volumes of fluids within microchannels. When scaling down to the microscale, fluid dynamics are dominated by laminar flow, characterized by smooth and ordered fluid motion with minimal mixing between adjacent layers. This behavior is governed by the low Reynolds number typical of microfluidic systems, where viscous forces dominate over inertial forces. Equation 1.1 defines the Reynolds number (Re), where ρ is the fluid density, v is the characteristic velocity, L is the characteristic length (such as channel width) and μ is the viscosity of the fluid.

$$Re = \frac{\rho v L}{\mu} \tag{1.1}$$

Laminar flow occurs when $Re < 2000$ [33] and it allows for precise control over the movement of fluids, enabling the creation of well-defined gradients of nutrients, oxygen and signaling molecules within the microchannels. This is particularly important for cell culture applications, as it allows for the establishment of microenvironments that can influence cell differentiation, proliferation and function.

OoC systems typically combine cell culture chambers and microfluidic channels in order to recreate the complex microenvironments found in living tissues. Culture chambers are designed to host cells or organoids, providing a three-dimensional environment that allows growth and interaction. In order to achieve compartmentalization of the chambers, one of the possibilities is the use of porous membranes, which allow selective exchange of molecules between adjacent channels while maintaining physical separation. Alternatively, membrane-free approaches can be employed using extracellular matrix gels or micropillar arrays, which provide structural support and promote cell-cell communication without the need for a physical barrier. These structures are connected through microfluidic networks composed of channels, valves and pumps that facilitate the controlled flow of culture medium and other fluids throughout the system, simulating for example blood circulation.

Microchannels can be designed with various geometries and dimensions to accommodate different cell types and experimental requirements, for instance including pillars or trenches to promote cell adhesion. In general, they can be manufactured in glass, silicon or polymers, depending on the desired properties and application. Different fabrication techniques include bulk or surface micromachining, especially for silicon and glass, and soft lithography for polymers like PDMS. Bulk micromachining involves the removal of material from a substrate to create three-dimensional structures, while surface micromachining builds up structures layer by layer on the substrate surface. Soft lithography, on the other hand, uses a master mold to replicate microchannel patterns in a polymer material, enabling fast and cost-effective prototyping. For what concerns cell culture applications, PDMS is widely used due to its biocompatibility, optical transparency and ease of fabrication. Nevertheless, glass can be used as a base material for stable channel fabrication.

Advanced configurations of microfluidic platforms may include pneumatic or mechanical actuators for dynamic perfusion, ensuring controlled shear stress and nutrient delivery. In addition, many platforms embed sensing elements such as microelectrodes, cantilevers or optical sensors to monitor parameters like pressure, oxygen concentration, and electrical activity in real time. These features allow

continuous observation of cellular responses without disrupting the experimental setup.[31]

1.1.3 In-liquid biosensing

In-liquid biosensing refers to the detection and analysis of biological molecules or cells directly within a liquid environment, such as bodily fluids (blood, saliva, urine) or culture media. This approach is particularly advantageous for real-time monitoring of biological processes, as it allows for continuous observation of dynamic changes in the sample without the need for extensive sample preparation or extraction. In-liquid biosensors can be integrated into microfluidic platforms, enabling precise control over fluid flow and sample handling, which is essential for maintaining the integrity of biological samples and ensuring accurate measurements.[2]

A biosensor is a analytical device that combines a biological recognition element with a transducer to convert a biological response into a measurable signal. The biological recognition element can be an enzyme, antibody, nucleic acid or cell receptor, which specifically interacts with the target analyte. The transducer then converts this interaction into an electrical, optical or mechanical signal that can be quantified. In-liquid biosensors can utilize various transduction mechanisms, including electrochemical, optical and piezoelectric methods.[2] Figure 1.2 illustrates a schematic representation of a biosensor, highlighting its main components.

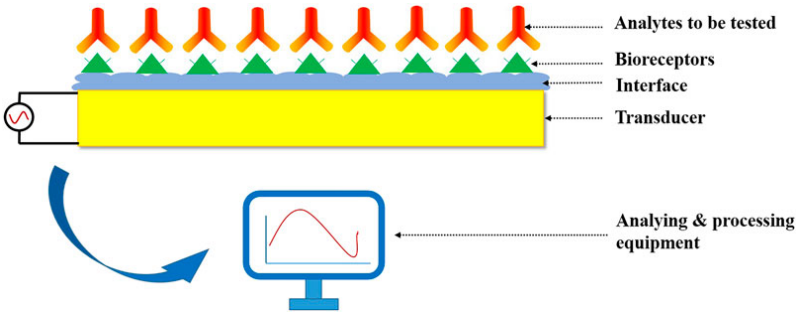

Figure 1.2: Schematic representation of a biosensor. Reproduced from Song et al.[2], licensed under CC BY.

1.2 Organic Electrochemical Transistors

Organic Electrochemical Transistors (OECTs) are a class of transistors that utilize organic semiconducting materials and operate based on the modulation of their conductivity through ionic interactions with an electrolyte. They have gained significant attention in recent years due to their unique properties, such as low operating voltages, biocompatibility, and the ability to interface with biological systems [34].

OECTs can be considered ad a subset of Organic Thin-Film Transistors (OTFT), which are transistors that use organic semiconducting materials in their active layer, category which comprehends also Organic Field-Effect Transistors (OFET) [26]. A different classification of OECTs is based on the type of insulating layer used in the device structure. In OECTs, the insulating layer is replaced by an electrolyte, which allows for the modulation of the channel conductivity through ionic interactions. With this idea in mind, OECTs can be classified as a type of Electrolyte-Gated Organic Transistors (EGOTs), as an alternative to Electrolyte-Gated Organic Field Effect Transistors (EGOFETs) [35].

1.2.1 From MOSFETs to OECTs

In order to understand the working principle of OECTs, it is useful to first review the operation of traditional Metal Oxide Semiconductor Field Effect Transistors (MOSFETs). A field-effect transistor (FET) is a type of transistor that controls the flow of current between two terminals (source and drain) by applying a voltage to a third terminal (gate). In the case of MOSFETs, the gate terminal is separated from the channel, where carriers flow generating the current, by a thin insulating layer, typically constituted by silicon dioxide. MOSFETs are planar devices fabricated on a silicon substrate, depending on the type of doping of source and drain, they can be classified as n-channel or p-channel MOSFETs. To form an n-channel MOSFET, the source and drain regions are heavily doped with n-type impurities (which provide extra electrons), while the substrate is typically slightly p-type (which has an abundance of holes). Conversely, for a p-channel MOSFET, the source and drain are doped with p-type impurities and the substrate is n-type. The classification of the channel as n- or p-type depends on the type of charge carriers that primarily conduct current through the channel: electrons for n-channel and holes for p-channel MOSFETs. The channel carriers correspond to majority carriers for source and drain regions, while they are minority carriers in the substrate.

MOSFETs are threshold devices, since conduction between source and drain occurs only when the gate-source voltage V_{GS} satisfies a certain threshold voltage V_{th}. The operation of these devices can be described by distinguishing three conditions based on the applied gate voltage:

- accumulation, when the gate voltage is such that majority carriers are attracted to the semiconductor-insulator interface, increasing the channel conductivity;
- depletion, when the gate voltage repels majority carriers from the interface between semiconductor and insulator, reducing the channel conductivity;
- inversion, when the gate voltage is sufficiently strong to attract minority carriers to the semiconductor-insulator interface, forming a conductive channel

that allows current flow between source and drain.

These three conditions depend on the type of MOSFET (n- or p-channel) and the polarity of the applied gate voltage. The threshold voltage V_{th} is the gate voltage at which the transition from depletion to inversion occurs, it is positive for n-MOSFETs and negative for p-MOSFETs. The voltage value that separates accumulation and depletion is named flat-band voltage V_{FB}, which is typically negative for n-MOSFETs and positive for p-MOSFETs.

In this context, the operation of p-MOSFET is presented, since the OECTs used in this work are p-type devices. Depending on the applied voltages, the p-MOSFET can operate in different regimes[36], keeping in mind that in this case $V_{th} < 0$ V and $V_{FB} > 0$ V:

- Cut-off region: when $V_{th} < V_{GS} < V_{FB}$, the channel is depleted and there is no conduction between source and drain ($I_D \approx 0$).
- Triode mode: when $V_{GS} < V_{th}$ a conductive channel forms, allowing current to flow between source and drain. The drain current I_D increases linearly with V_{DS} according to the Equation 1.2, where μ_p is the carriers (holes) mobility, C_{ox} is the capacitance per unit area of the gate oxide, W and L are the width and length of the channel, respectively, and λ is the channel-length modulation parameter.

$$I_D = -\mu_p C_{ox} \frac{W}{L} \left[(V_{GS} - V_{th}) V_{DS} - \frac{V_{DS}^2}{2} \right] [1 - \lambda V_{DS}] \tag{1.2}$$

- Saturation region: when $V_{GS} < V_{th}$ and $|V_{DS}| > |V_{DS,sat}|$, the channel near the drain becomes pinched off, leading to a saturation of the drain current I_D, which becomes relatively constant with increasing V_{DS}, as expressed by Equation 1.3, where $V_{DS,sat} = V_{GS} - V_{th}$ is the drain-source voltage at the onset of saturation.

$$I_D = -\frac{1}{2} \mu_p C_{ox} \frac{W}{L} (V_{GS} - V_{th})^2 [1 - \lambda V_{DS}] \tag{1.3}$$

The typical electrical characteristics of a p-MOSFET are shown in Figure 1.3: the transfer characteristics represents the behavior of the drain current I_D with respect to the gate-source voltage V_{GS} at a constant drain-source voltage V_{DS}, while the output characteristics is the plot of the drain current I_D vs drain-source voltage V_{DS}, computed for different gate-source voltages V_{GS}. Note that the x-axis of the transfer characteristics is inverted, since it is a p-type device. The transition from the linear (triode) region to the saturation region is indicated. In any case, the gate current I_G in MOSFETs is ideally zero, since the gate is insulated from the channel by the oxide layer.

The MOSFET technology is nowadays well established and widely used in electronics, being the fundamental building block of modern integrated circuits, due to its high performance, low power consumption, scalability and integration possibilities. However, MOSFETs are rigid devices fabricated on inorganic semiconductor substrates, which limits their application in flexible and wearable electronics. This limitation has driven the development of alternative transistor technologies,

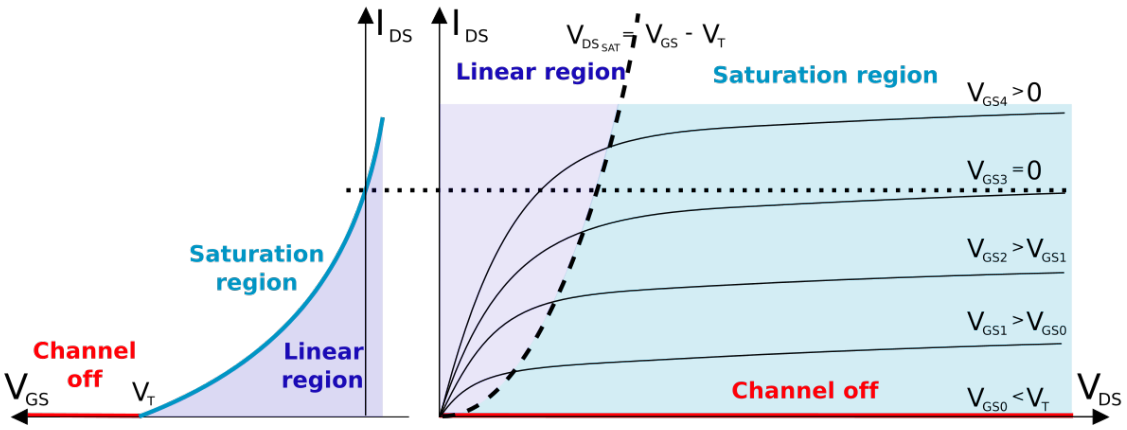

Figure 1.3: Typical transfer and output characteristics of a p-MOSFET, showing the drain current I_D as a function of the drain-source voltage V_{DS} for different gate-source voltages V_{GS}. Reproduced from[3], licensed under CC BY-SA 4.0.

such as OECTs, which utilize organic semiconducting materials and offer advantages in terms of flexibility, biocompatibility, low-voltage operation, cost and ease of fabrication, making them suitable for biomedical applications. OECTs share a similar three-terminal structure with MOSFETs, consisting of source, drain and gate electrodes. However, in OECTs, the insulating layer between gate and channel is replaced by an electrolyte, which allows for ionic conduction and interaction with the organic semiconductor channel. The channel material in OECTs is typically an organic mixed ionic-electronic conductor (OMIEC), such as poly(3,4-ethylenedioxythiophene) polystyrene sulfonate (PEDOT:PSS). Figure 1.4 schematically illustrates the differences between a MOSFET and a OECT.

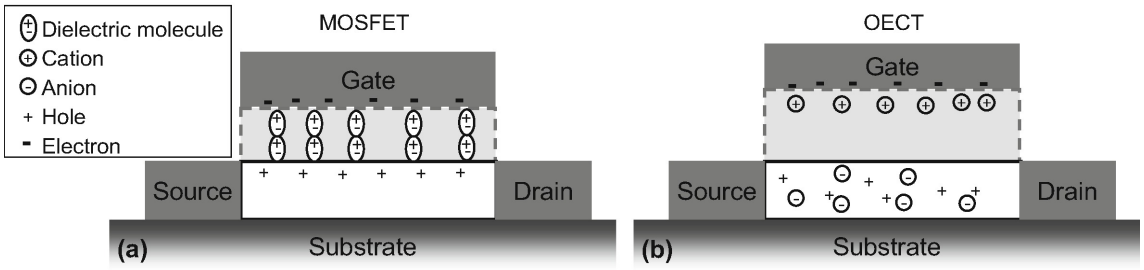

Figure 1.4: Schematic comparison between MOSFET and OECT. In the MOSFET, the gate electrode is separated from the channel by an insulating oxide layer, while in the OECT, the gate electrode is in contact with an electrolyte that interfaces with the organic semiconductor channel. The operation of both devices relies on the modulation of channel conductivity through the application of a gate voltage, but the mechanisms differ due to the presence of the electrolyte and the organic semiconductor in OECTs. Reproduced from[4], licensed under CC BY.

Different architectures can be employed for OECTs, depending on the configuration of the electrodes and the electrolyte. Figure 1.5 shows four common OECT architectures:

- bottom contact, where the source and drain electrodes are fabricated on the

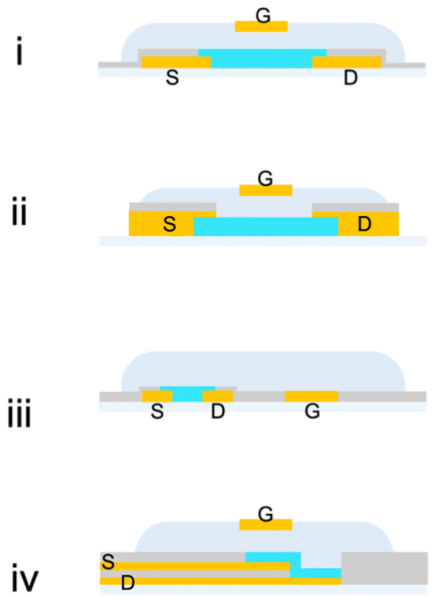

Figure 1.5: Different architectures of OECTs: i) bottom contact, ii) top contact, iii) coplanar and iv) vertical. Adapted from Ohayon et al.[5], licensed under CC BY.

substrate before depositing the organic semiconductor channel;

- top contact, where the source and drain electrodes are deposited on top of the organic semiconductor channel;
- coplanar, where the source, drain and gate electrodes are all fabricated on the same plane;
- vertical, where the source and drain electrodes are stacked vertically and separated by an insulating layer.

The bottom contact is the most common and it presents a faster switching capability with respect to the top contact case, which instead appears to be preferable for what concerns reproducibility of the devices. In both cases the gate contact is dipped into the electrolyte above the channel, in an out-of-plane configuration. On the other hand, the coplanar gate configuration is more practical as there are no separate components. The vertical case is the most recent, it allows a smaller footprint and a reduced channel length, improving transconductance and switching speed of the device.[5]

1.2.2 OECT working principle

OECTs are transistors in which the channel is made of an organic semiconductor and it is separated from the gate terminal by an electrolyte, as schematized in Figure 1.4. The basic idea behind the operation of OECTs is the penetration of ions from the electrolyte solution into the organic semiconductor channel, changing its doping state and thus modulating its conductivity. The gate voltage is therefore responsible for the doping state of the channel, increasing or reducing the number of charge carriers available for conduction. Figure 1.6 shows a schematic representation

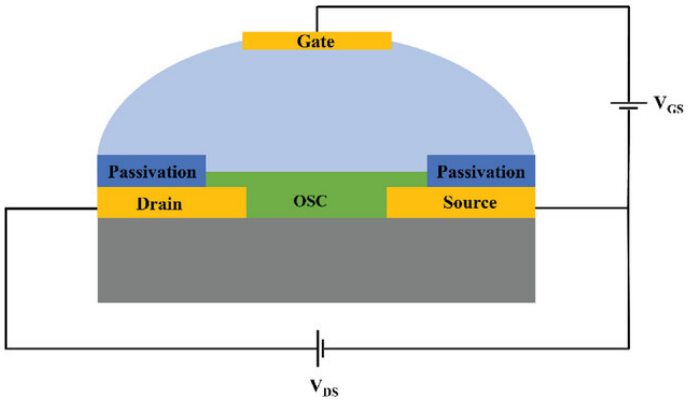

Figure 1.6: Schematic representation of an Organic Electrochemical Transistor (OECT) structure. Reproduced from Segantini et al.[6], licensed under CC BY.

of an OECT structure, indicating the three terminals (source, drain and gate), the organic semiconductor (OSC) channel and the electrolyte layer.

A typical material used for the channel in OECTs is PEDOT:PSS, which is a *p*-type organic mixed ionic-electronic conductor (OMIEC). In this configuration, the OECT operates as a depletion-mode device, meaning that it is normally on (conductive) when no gate voltage is applied, and it can be turned off (non-conductive) by applying a positive gate voltage. A positive gate bias drives cations from the electrolyte into the PEDOT:PSS channel, compensating the negative charges on the PSS chains and reducing the number of holes in the PEDOT chains. This process is equivalent to compensation doping in silicon technology, it is known as dedoping and it leads to a decrease in the channel conductivity, effectively turning off the transistor. Conversely, when a negative gate voltage is applied, cations are repelled from the channel, allowing it to remain in its doped state with a high concentration of holes, resulting in high conductivity and turning on the transistor. These behavior is schematized in Figure 1.7, where panel a) shows the OECT at zero gate bias, with high channel conductivity due to the doped state of the organic semiconductor and therefore the large presence of holes available for conduction, while panel b) illustrates the OECT under positive gate bias, with reduced channel conductivity due to dedoping caused by cation injection from the electrolyte into the channel.[34;7]

The opposite behavior is observed in accumulation-mode OECTs, which are made of organic semiconductors that present normally a small number of charge carriers, being therefore non-conductive at zero gate bias. In this case, the application of a negative gate voltage leads to the injection of anions into the channel, causing accumulation of holes and increasing the channel conductivity, turning on the transistor. Differently from MOSFETs, in OECTs the doping modification occurs over the whole volume of the organic semiconductor channel, not only at the interface with the electrolyte. This volumetric doping leads to a larger modulation of the drain current achieved with low gate voltages, compared to traditional FETs, making OECTs highly sensitive to changes in the electrolyte composition.[34]

Bernards and Malliaras[7] derived a model to describe the steady-state and transient characteristics of a depletion-mode OECT, which is considered as the union of an electronic circuit and an ionic circuit. The electronic circuit describes the holes transport in the organic semiconductor channel according to Ohm's law, as expressed in Equation 1.4, where $J(x)$ is the current density at position x along the

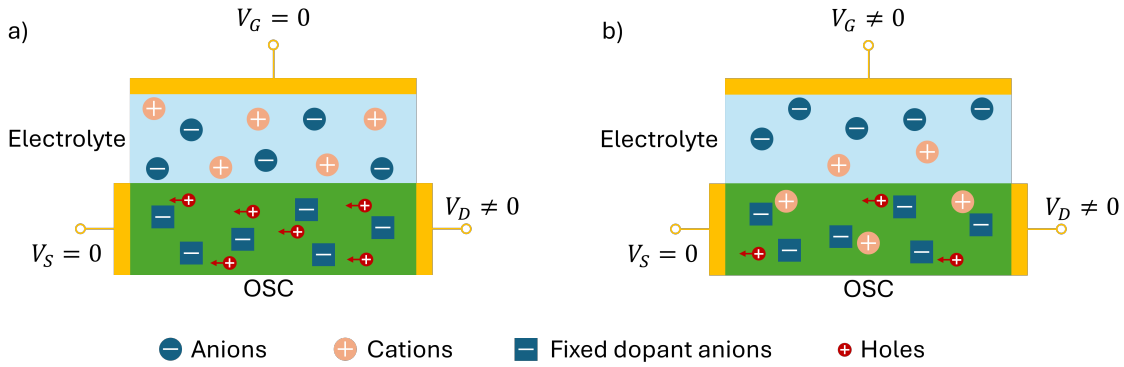

Figure 1.7: Schematic representation of depletion-mode OECT behavior with applied drain voltage. a) OECT at zero gate bias, with high channel conductivity due to the doped state of the organic semiconductor. b) OECT under positive gate bias, with reduced channel conductivity due to dedoping caused by cation injection from the electrolyte into the channel. Adapted from Bernards and Malliaras.[7].

channel, q is the elementary charge, μ_p is the hole mobility (assumed constant), $p(x)$ is the hole concentration at position x and $V(x)$ is the electric potential at position x.

$$J(x) = q\mu_p p(x)\frac{dV(x)}{dx} \tag{1.4}$$

The effective dopant density p in the semiconductor material is computed as expressed in Equation 1.5, where p_0 is the initial hole concentration in the channel at zero gate bias, Q is the total ionic charge injected into the channel from the electrolyte and v is the volume of the channel.

$$p = p_0\left(1 - \frac{Q}{qp_p v}\right) \tag{1.5}$$

The ionic circuit, on the other hand, represents the ionic charge motion in the electrolyte as a series of a resistor and a capacitor. The resistor R_s accounts for the ionic resistance of the electrolyte, while the capacitor C_d represents the capacitance at the interface between OSC and electrolyte and between gate and electrolyte, due to polarization. Considering a differential portion dx of the channel around position x, when a gate voltage V_G is applied, after a certain transit time the charge injected into the channel can be expressed as in Equation 1.6, where c_d is the ionic circuit capacitance per unit area, W is the channel width and $V(x)$ is the electric potential at position x.

$$Q(x) = c_d W dx\,(V_G - V(x)) \tag{1.6}$$

The OECT characteristics at steady-state can be described by Equation 1.7, where $V_p = qp_0T/c_d$ is the pinch-off voltage (T is the OSC thickness).

$$J(x) = q\mu_p p_0\left[1 - \frac{V_G - V(x)}{V_p}\right]\frac{dV(x)}{dx} \tag{1.7}$$

In steady-state conditions, placing the source in $x = 0$ and the drain in $x = L$, applying a gate voltage $V_G > 0$ the drain current I_D can be expressed as in Equation 1.8 depending on the applied drain-source voltage V_{DS}, with G representing the

conductance of the OSC, defined as $G = q\mu_p p_0(TW/L)$, and $V_{DS,sat} = V_G - V_p$ being the drain-source voltage at the onset of saturation. Three regimes of operation of the OECT can be identified, listed here in the same order as reported in Equation 1.8: uniform de-doping, partial de-doping (linear regime) and saturation.[7]

$$I = \begin{cases} G\left[1 - \dfrac{V_G - 1/2V_{DS}}{V_p}\right] V_{DS} & \text{if } |V_{DS}| < V_G \text{ and } |V_{DS}| < |V_{DS,sat}| \\ G\left(V_{DS} - \dfrac{V_G^2}{2V_p}\right) & \text{if } V_G < |V_{DS}| < |V_{DS,sat}| \\ \dfrac{GV_{DS,sat}^2}{2V_p} & \text{if } |V_{DS}| \geq |V_{DS,sat}| \end{cases} \tag{1.8}$$

In Figure 1.8, the typical curves and figures of merit of OECTs are presented. Figure 1.8A shows the output characteristics of an OECT, where the drain current I_D is plotted as a function of the drain-source voltage V_{DS} for different gate-source voltages V_{GS}. The pinch-off voltage V_p is indicated, which is the value that, together with the applied gate voltage V_{GS}, determines the transition from the linear to the saturation region. Figure 1.8B displays the transfer characteristics of the OECT, showing the drain current I_D as a function of the gate-source voltage V_{GS} at a constant drain-source voltage V_{DS}. The ON/OFF ratio and threshold voltage V_{th} can be extracted from this plot as illustrated. Figure 1.8C illustrates the hysteresis observed in the transfer characteristics of an OECT, which can be attributed to a different ion penetration and extraction dynamics during the forward and reverse gate voltage sweeps. Finally, Figure 1.8D presents a plot of the transconductance g_m as a function of channel geometry and gate voltage, where the slope corresponds to the product of mobility μ and volumetric capacitance C^*, which are key parameters for evaluating OECT performance.[5]

1.2.3 Applications in biosensing

OECTs are well suited for biosensing applications because of their stability in aqueous environments, low operating voltages, high sensitivity and biocompatibility. They have been employed as recording and stimulation devices, enabling the monitoring of electrophysiological signals from cells and tissues, such as action potentials from neurons or cardiac cells. They can be used in complex environment allowing detection of biomolecules in electrolytes or body fluids, demonstrating their potential for early detection of diseases and real-time health monitoring.[37]

The principle behind biosensing with these devices lies in the modification of the potential drop across the interface between the gate and the electrolyte or between the electrolyte and the organic semiconductor channel, caused by the presence of specific biological analytes. This potential change affects the doping state of the channel, leading to a modulation of the drain current that can be correlated to the concentration of the target analyte. The selectivity of the sensor is typically achieved by functionalizing the gate electrode or the channel surface with specific recognition elements, such as antibodies, aptamers or molecularly imprinted polymers, which bind selectively to the target analyte. The binding of the analyte to the recognition element causes changes in the local ionic environment, leading to a modulation of the channel conductivity and thus the drain current. This change can be measured and correlated to the analyte concentration.[26]

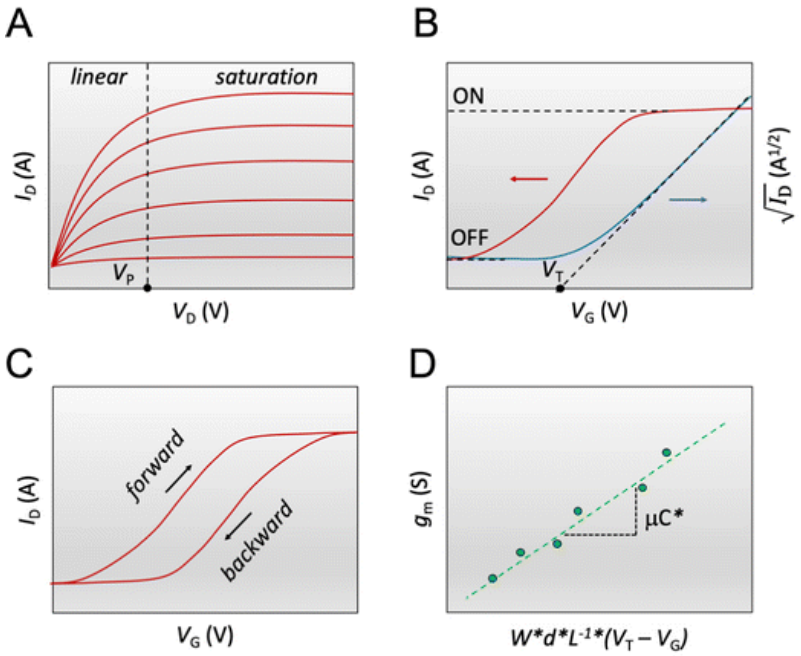

Figure 1.8: Steady-state figures of merit for OECTs. (A) Output curves showing I_D vs. V_D at different constant V_G; (B) Transfer curve with ON/OFF ratio and V_{th} computation; (C) Hysteresis in transfer characteristics; (D) Plot of g_m vs. channel geometry, where the slope corresponds to the μC^* product. Reproduced from Ohayon et al.[5], licensed under CC BY.

A typical use of OECTs consist in enzymatic sensors, where enzymes immobilized on the gate electrode catalyze the substrate into products that exchange electrons with the electrode. This electron transfer generates an electrical signal at the gate, which modulates the channel current. To maintain overall charge neutrality in both the ionic and electronic circuits, cations penetrate the conducting polymer film, replacing $PEDOT^+$ in compensating PSS^-. This process shifts the effective gate voltage, causing a decrease in channel current that is related to the substrate concentration. The sensitivity of OECT devices depends on the intrinsic amplification provided by optimized geometry and enzymatic functionalization.[8] Another common application of OECTs is in immunosensors, where antibodies or antigens are immobilized on the gate electrode or channel surface to specifically bind target biomolecules. The binding event induces changes in the local ionic environment, leading to a modulation of the channel conductivity and thus the drain current. This change can be measured and correlated to the concentration of the target analyte. Similarly, single stranded DNA probes can be immobilized on the gate to specifically hybridize with complementary DNA sequences, enabling the detection of specific genetic markers or pathogens.[8;37] A rather recent application of OECTs in biosensing is in cell-based sensors, where living cells are cultured directly on the channel surface. The interaction between the cells and the organic semiconductor can lead to changes in the channel conductivity, which can be monitored in real-time. This approach allows for the study of cellular responses to various stimuli, such as drugs or toxins, and has potential applications in drug screening and toxicity testing.[38]

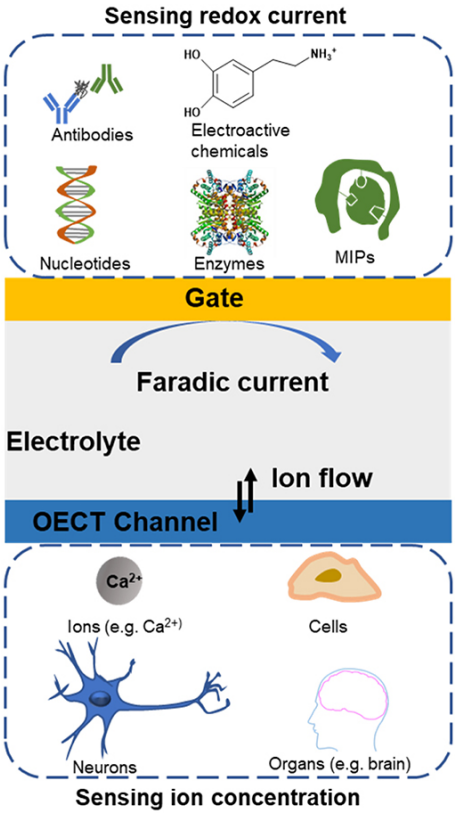

Figure 1.9: Schematic overview of biological applications with OECTs. Reproduced from Bai et al.[8], licensed under CC BY.

1.3 Organic semiconductors

Organic semiconductors (OSCs) are a class of materials that possess semiconducting properties due to their molecular structure, which typically consists of conjugated systems with alternating single and double bonds. These materials can be small molecules, oligomers or polymers and are characterized by their ability to conduct electricity through the movement of charge carriers (electrons and holes) along the conjugated backbone. Figure 1.10 shows some examples of common organic semiconductors.

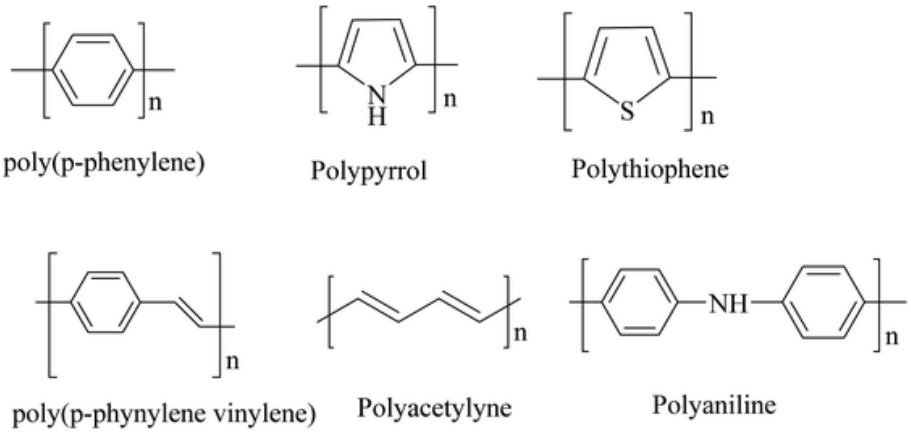

Figure 1.10: Examples of common organic semiconductors. Reproduced from K and Rout[9], licensed under CC BY.

OSCs have gained significant attention in recent years due to their potential applications in flexible electronics, organic light-emitting diodes (OLEDs), organic photovoltaics (OPVs) and organic transistors. Their advantages include mechanical flexibility, low-cost fabrication processes (such as solution processing and printing techniques), and tunable electronic properties through chemical synthesis. However, OSCs typically exhibit lower charge carrier mobilities and stability compared to inorganic semiconductors. One of the most interesting properties of OSC is the tunable and temperature-dependent conductivity: the conductivity depends on the temperature since the transport is assisted by phonons, but it can be modified introducing doping to change the states available for conduction, which is obtained through reversible oxidation or reduction reactions.[10]

1.3.1 Physics of conjugated polymers

Conjugated polymers (CPs) are a subset of OSCs that consist of long chains of repeating monomer units with alternating single and double bonds, creating a conjugated system. This conjugation allows for the delocalization of π-electrons along the polymer backbone, which is crucial for their semiconducting properties. Figure 1.11 shows a schematic representation of a conjugated polymer chain.

Organic polymers have carbon atoms as their main constituents, which have four valence electrons. In conjugated polymers, three of these electrons form strong σ-bonds with neighboring atoms, creating the polymer backbone. The fourth electron occupies a p_z-orbital that is perpendicular to the plane of the σ-bonds. These

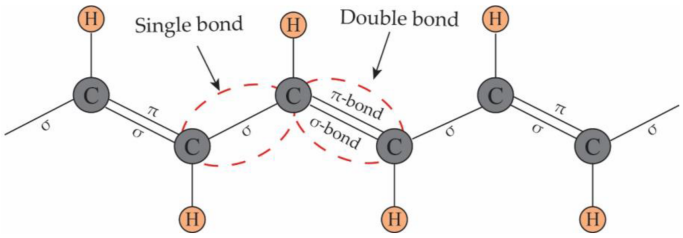

Figure 1.11: Representation of a conjugated polymer (polyacetylene) chain with alternating single and double bonds, illustrating the delocalized π-electron system along the backbone. Reproduced from Le et al.[10], licensed under CC BY.

p_z-orbitals lead to the formation of π-bonds through side-to-side overlap with adjacent p_z-orbitals along the polymer chain. Between these bonds, the low-energy bonding states correspond to the inorganic semiconductors valence band, while the high-energy antibonding states correspond to the conduction band. The highest energy state between the bonding states is the HOMO (Highest Occupied Molecular Orbital), while the lowest energy state of the antibonding ones is the LUMO (Lowest Unoccupied Molecular Orbital). The energy gap of OSC is defined as the energy difference between LUMO and HOMO. When multiple p-orbitals overlap along the polymer chain, they form a delocalized π-electron system, which is responsible for the semiconducting properties of CPs.[39;10]

CP can be p- or n-type meaning that they can transport injected holes or electrons, respectively. The concept of doping in OSCs is related to REDOX (reduction-oxidation) reactions: reduction is the gain of electrons or a decrease in oxidation state, while oxidation is the loss of electrons or an increase in oxidation state. In this view, the n-doping for an OSC is called reduction doping and p-doping is oxidation doping, which is more stable because of the oxidizing nature of the atmosphere (containing oxygen). Doping can be interstitial, electrochemical, photochemical or molecular.[10]

Polymer semiconductors do not present a crystal structure, but rather a semi-crystalline or amorphous arrangement of polymer chains. A hole (or electron) transporting material exhibits a set of hole (or electron) states corresponding to conjugation sites distributed in space and energy. This disordered condition prevents charge carriers from moving freely as in crystalline inorganic semiconductors. Instead, charge transport in CPs occurs via a hopping mechanism, where charge carriers jump between localized states on different polymer chains or segments through thermally-assisted quantum mechanical tunneling. This process is less efficient than band transport in crystalline materials, leading to lower charge carrier mobilities in CPs compared to inorganic semiconductors. The hopping rate depends on factors such as the distance between localized states and their energies, parameters which are represented through the density of states (DOS) of the material. Introducing disorder in the system causes the localization of electronic states, which in crystals are delocalized in bands. The DOS in disordered CPs is often modeled using Gaussian or exponential distributions.

When an electric field is applied to the CP, the potential profile in the material changes according to the Poole-Frenkel effect, which states the proportionality of the barrier lowering to the electric field. The decrease of the energy barrier due to the applied field improves the hopping probability of the carriers, increasing the

mobility and thus the conductivity of the material.[4]

1.3.2 PEDOT:PSS

The most popular material for OECT channel fabrication is PEDOT:PSS, poly(3,4-ethylenedioxythiophene) polystyrene sulfonate (Figure 1.12), a polymer blend consisting of the conductive polymer PEDOT and the polyelectrolyte PSS. PEDOT:PSS is widely used due to its high conductivity and ease of processing from aqueous dispersions, which are prepared by polymerizing the EDOT monomer in the presence of PSS.[34] Moreover, it exhibits good stability in ambient conditions and biocompatibility, making it suitable for bioelectronic applications[40].

PEDOT:PSS is a *p*-type CP, meaning that it has a high concentration of holes (positive charge carriers) states available for conduction, due to the compensating effect of the sulfonate groups in PSS on the mobile holes in PEDOT[37]. The conductivity of PEDOT:PSS can reach up to 4000 S/cm[5].

In the context of this work, PEDOT:PSS is used as the channel material in organic electrochemical transistors (OECTs) due to its mixed ionic-electronic conduction properties, which allow for efficient modulation of the channel conductivity through ionic interactions with the electrolyte[5].

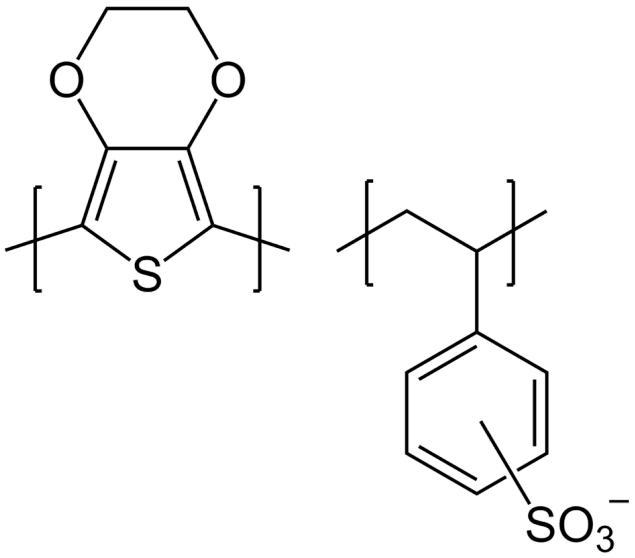

Figure 1.12: PEDOT:PSS polymer structure.

Chapter 2

Materials and Methods

All the fabrication steps, microfluidic tests and electrical characterizations were performed in laboratories of DiSAT ("Dipartimento di Scienza Applicata e Tecnologia") department in Politecnico di Torino, located in INRiM (Istituto Nazionale di Ricerca Metrologica) site (Strada delle Cacce 91, Turin, Italy), in particular:

- Microfluidics laboratory,
- Electrical measurements laboratory,
- Additive Manufacturing laboratory,
- Synthesys and Additive Manufacturing laboratory,
- PiQuET clean room facility, shared by INRiM, Politecnico di Torino and Università degli Studi di Torino[41].

The colture of the cell barrier model is managed in the Interdepartmental Center PolitoBIOMed Lab, the Biomedical Engineering laboratory at Politecnico di Torino (Via Pier Carlo Boggio 59, Turin, Italy)[42]. PolitoBIOMed Lab provided two membranes to be used in the platform: a commercial one (*Unique-Mem® Track-Etched Membranes*, Oxyphen AG, Wetzikon, Switzerland) and one produced by *KLISBio S.r.l.* (Bresso, Italy).

2.1 Design of the multi-layer microfluidic platform

2.1.1 Version 0: initial stage of the project

The project was designed using CAD software *Rhinoceros 8*[43]. Figure 2.1 shows the initial design of the microfluidic platform, which is composed by two layers represented here with two different colors. The whole device has rectangular footprint with sides of 22 mm and 60 mm (Figure 2.2a). As reported in Figure 2.2b, both layers are 1.5 mm thick and incorporate a microfluidic channel measuring 0.7 mm in width and 1 mm in height (Figure 2.2c). Each channel extends from one edge of the platform to the opposite one, passing through a central chamber that is 6.5 mm wide and open on both sides. The chamber is octagon-like shaped, which allows an easier flowing of the liquid in the desired direction, compared to a circular shape. A

thin membrane is placed between the two layers in the central region to separate the channels and act as support for cell culture. In order to avoid leakages, the central hole is closed on both sides with a 3D-printed plug, built with a transparent material to allow seeing the medium flow below it. The central plug was initially designed with a thickness of 0.5 mm, but after some microfluidic leak tests (Section 3.2.1, Figure 3.6b) it was modified to 0.7 mm in order to achieve better sealing thanks to a more stable mechanical interlock. The inlet and outlet of each channel are obtained by perforating the top layer using a biopsy punch with 1 mm diameter.

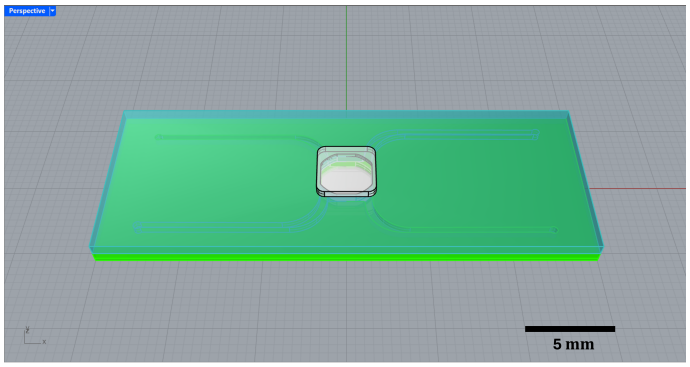

Figure 2.1: CAD design of the microfluidic platform at the initial stage of the project.

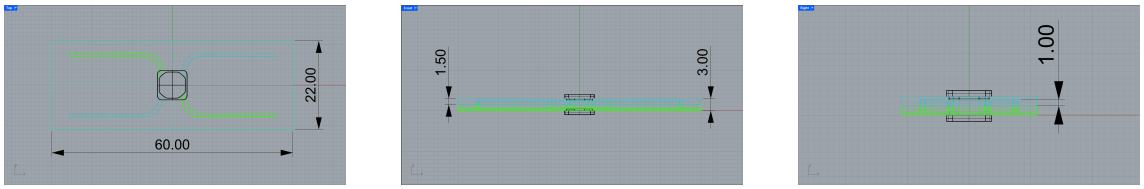

(a) Top view. (b) Front view. (c) Right view.

Figure 2.2: Different views of the initial CAD design with dimensions (in mm).

The version 0 of the design is perfectly symmetrical and therefore easy to fabricate; however, this configuration does not allow proper integration of the OECT sensors and does not provide enough space for culturing a real barrier model. For these reasons, the layout was modified to include a higher central chamber and dedicated allocations for the OECTs connected to the microfluidic channels.

2.1.2 Version 1: multi-layer platform for commercial membrane

Version 1 of the platform, reported in Figure 2.3, has been drawn considering a very thin commercial membrane to be placed between the top and bottom layers. The chosen *Unique-Mem® Track-Etched Membrane* (Oxyphen AG, Wetzikon, Switzerland) is a PC (Polycarbonate) sheet with 0.4 µm cylindrical pores, it is chemically resistant and biologically inert therefore it is suitable for cell culture applications [19]. The technical specifications of the commercial membrane are reported in Table 2.1, reproduced from the manufacturer official website [19]. In order to ensure uniform closure of the device, the thickness of the membrane must be taken into account,

therefore it was measured using a KLA P-17 profilometer. The obtained results indicate that the commercial membrane has a thickness of approximately (38 ± 3) µm, which is consistent with the range indicated in Table 2.1 going from 8 µm to 50 µm. In this case the sheet is thin enough to be inserted directly between the two layers of the microfluidic platform without requiring structural modifications.

Specification	**Value**
Bandwidth (mm)	10, 13, 14.5, 20 and customized dimensions
Materials	PET – slightly hydrophilic; PC – slightly hydrophobic
Pore size range	0.1 µm – 10 µm
Pore density	From 10^3 to 10^9 pores/cm^2
Thickness	From 8 µm to 50 µm
Operating temperature	From -40°C to 160°C (up to 200°C for special applications)
Air flow	Up to 800 l/(bar cm^2 min)
Hydrophilic treatments	Various treatments to enhance wettability and water flow (e.g., PVP treatment)
Hydrophobic/oleophobic treatments	Up to grade 7.5; according to AATCC TM118
Salt spray resistance test	IEC60068-2-52, customer validation
Temperature resistance test	ISO16750-4 (ongoing)
Thermal shock test with ice water	ISO16750-4 (ongoing)
Climate resistance test	ISO16750-4
Chemical resistance test	LV124 / ISO16750-5
IP protection	IP64/65/66/67/68 according to DIN40050

Table 2.1: Technical Specifications of Unique-Mem® Track-Etched Membranes, table reproduced from Oxyphen official website [19]

As highlighted in Figure 2.4b, the top layer has been heightened to 4 mm in order to have space for an approximately 3 mm thick *in vitro* biological model to be cultured above the membrane in the central chamber. The bottom layer thickness was not modified with respect to the initial stage, represented in Figure 2.2b, and neither was the channels height, but some little chambers were added in correspondence of the OECTs to allow the connection with the microfluidic channels, with total heights of 2.50 mm for the top layer and 1.50 mm for the bottom one, as reported in Figure 2.4b. Moreover a filling channel has been designed to have a direct access to the part of the central chamber which is underneath the membrane. This additional channel needs to be sealed during culture, therefore a plug was designed with a decreasing square section, that in the middle length presents a side of 1 mm like the filling channel section, as indicated in Figure 2.4a. Lastly, a 1.5 mm thick layer ("closing layer") was added below the bottom layer to seal the bottom part of the central chamber and host the OECTs and the electrodes in specific compartments so that they are aligned with the holes in the bottom layer, allowing for the culture medium to reach them. Figure 2.4a reports the sizes of the chips and gates that are integrated in the closing layer. On the top layer the removable plug

has been maintained since the barrier model requires air exposure after some days of culture.

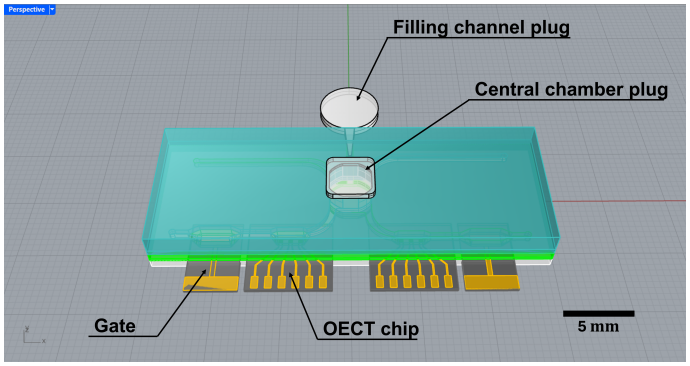

Figure 2.3: CAD design of the microfluidic platform at a second stage of the project.

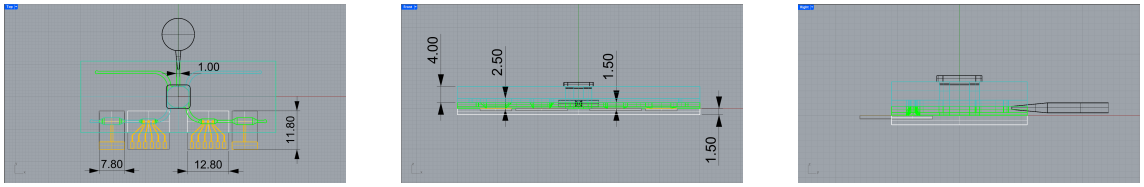

(a) Top view. (b) Front view. (c) Right view.

Figure 2.4: Different views of the second stage CAD design with dimensions (in mm).

2.1.3 Version 2: multi-layer platform for KLISBio Membrane

The alternative membrane to be integrated is a silk fibroin one, produced by *KLISBio S.r.l.* (Bresso, Italy), composed by a textile side and an electruspun layer. Silk possesses properties such as excellent biocompatibility, tunable biodegradability and mechanical strength, which make it suitable for tissue engineering and biomedical applications[44]. Since no datasheet is available for this innovative product yet, its thickness was measured with a KLA P-17 profilometer. The KLISBio membrane resulted to be about (210 ± 10) µm thick, therefore a re-design was needed due to the higher thickness with respect to the PC one. Consequently, version 2 of platform, intended to host the silk fibroin membrane, was designed with a 200 µm deep excavation in the top layer to accommodate it. The depth of the excavation was chosen to be slightly less than the membrane thickness in order to ensure a good seal when the device is closed. An additional change was performed by prolonging the channels to the edge beyond the chambers above the sensors, so that the exit of the medium could be easier. In order to close those outlets two other plugs have been designed, similar to the one closing the filling channel but with rectangular section. The closing layer was extended beneath the integrated chips to provide mechanical support, preventing the device from bending when electrical probes were placed in contact with the pads. This modification was later integrated also in version 1 of

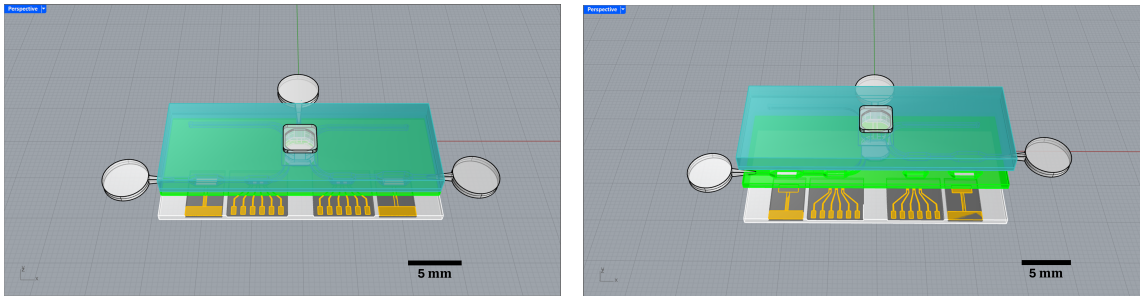

(a) Assembled view of the platform. (b) Disassembled view of individual layers.

Figure 2.5: CAD design of the alternative version of the platform for KLISBio 200 µm thick membrane, with side outlets of the channels.

the device, for the commercial membrane. This version of the design is reported in Figure 2.5.

2.2 Microfluidic platform fabrication

The multi-layer microfluidic platform was fabricated through replica molding. The masters were designed using CAD software *Rhinoceros 8* [43] and then 3D-printed with a PolyJet 3D printer (Stratasys J35™ Pro[45]). After cleaning and annealing them, liquid PDMS was cast into the molds and then put in the oven to achieve polymerization. Two bonding techniques were employed for assembling the different PDMS layers, in order to compare their performance: plasma bonding and adhesive bonding with a thin layer of uncured PDMS.

2.2.1 3D printing

Masters desing

The masters to be printed were designed as the complementary of the layers structures, with the same CAD software (*Rhinoceros 8* [43]). All the molds have a 3 mm thick base, above which the desired structure is built, with a frame which is as high as the wanted layer thickness. Figure 2.6 shows the structures to be 3D-printed for the fabrication of top (2.6a) and bottom (2.6b) layer of the platform that will be assembled with the thin commercial membrane in the middle. Figure 2.7 reports the corresponding designs for the alternative version of the platform, which will contain the thicker membrane. As explained in Section 2.1, in this case a 200 µm deep housing for the membrane was drawn in the top layers, which can be seen in Figure 2.7a, and the channels were extended to the lateral edges. In all the designs the structures that will correspond to the central and the small channel chambers are 0.5 mm higher than the frame, in order to get holes in the whole layer where desired. The closing layer in the end was chosen to be the same for both versions of the device, the corresponding master is represented in Figure 2.8, with 0.5 mm raisings to get the digs for the accommodation of the chips, which are usually fabricated on a 0.5 mm thick wafer.

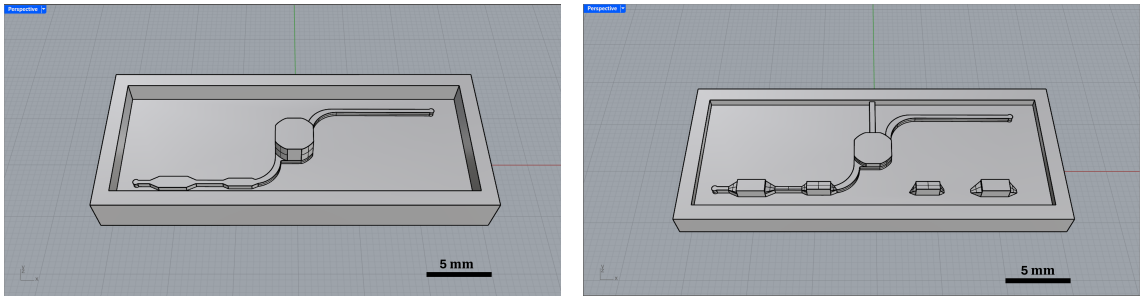

(a) Mold for top layer. (b) Mold for bottom layer.

Figure 2.6: CAD design of the masters to be 3D-printed to build the platform for the commercial membrane.

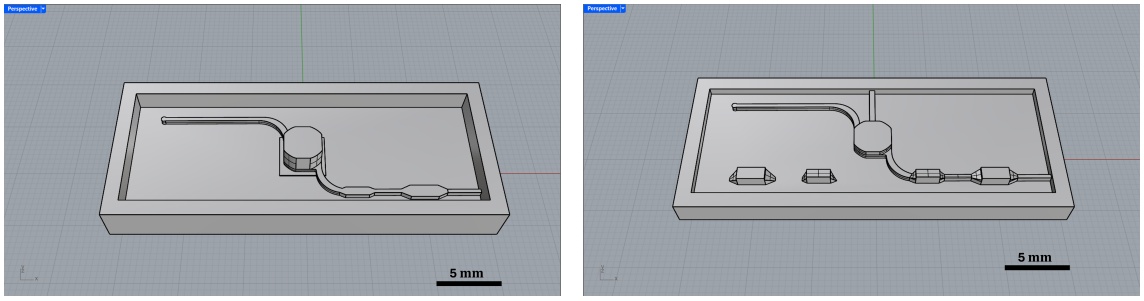

(a) Mold for top layer. (b) Mold for bottom layer.

Figure 2.7: CAD design of the masters to be 3D-printed to build the platform for KLISBio membrane.

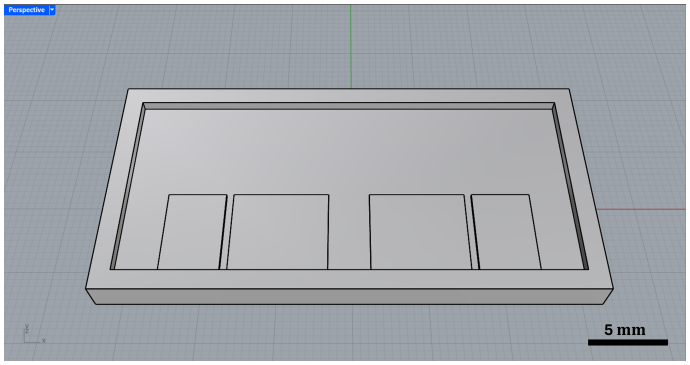

Figure 2.8: CAD design of the masters to be 3D-printed to build the closing layer of the platform.

3D printer

The designed structures were fabricated using a PolyJet 3D printer (Stratasys J35™ Pro,[45]). PolyJet printing technology is based on the layer-by-layer deposition of photopolymeric materials, which are then cured with ultraviolet (UV) light to form solid structures[46]. The printing heads, highlighted in Figure 2.9, jet thousands of photopolymer droplets which are cured by a UV lamp (Figure 2.9) during the fabrication process, while the building platform is lowered as the layers are formed. The printed sample is composed of the model material and it is delivered together with a support structure, made of a different material. The support is required during the printing process and is removed afterwards using water.[47;48]

The masters and the channel plugs (described in Section 2.1) were printed using VeroUltraWhite material by Stratasys[49], an opaque photopolymer. Alternatively, the central plug was fabricated using VeroUltraClear[50], a transparent material that mimics PMMA, allowing to see underneath when placed to seal the central chamber of the device.

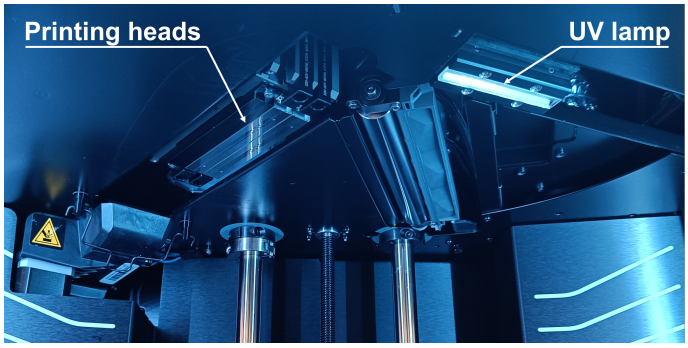

Figure 2.9: Close-up view of Stratasys J35™ Pro Printer elements.

Final step of the masters fabrication process

Figure 2.10 shows the printed masters for the fabrication of the three PDMS layers of the platform for KLISBio membrane. After extraction from the 3D printer and initial removal of the support material through water cleaning, the printed components were further cleaned using isopropyl alcohol (2-propanol) in a 10-minute ultrasonic bath and then they were placed in an oven overnight at 110°C. This step was essential to ensure proper PDMS casting and polymerization, since otherwise the PDMS curing could be inhibited, causing the elastomer to adhere to the printed model material and therefore get damaged during the replica molding process[51]. The final products for the three molds (version 2 of the platform) are shown in Figure 2.10, with the top layer mold in Figure 2.10a, the bottom layer mold in Figure 2.10b and the closing layer mold in Figure 2.10c. Figure 2.11 shows instead the 3D-printed plugs from top and frontal point of view: the central chamber tap in Figure 2.11a, the filling channel plug in Figure 2.11b and the lateral outlets plug in Figure 2.11c.

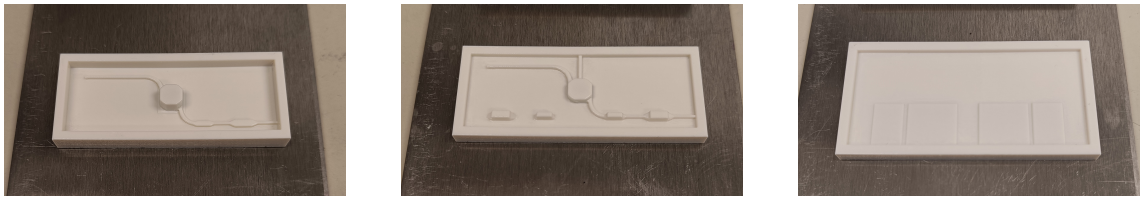

(a) Top layer. (b) Bottom layer. (c) Closing layer.

Figure 2.10: 3D-printed master molds for PDMS fabrication through replica molding.

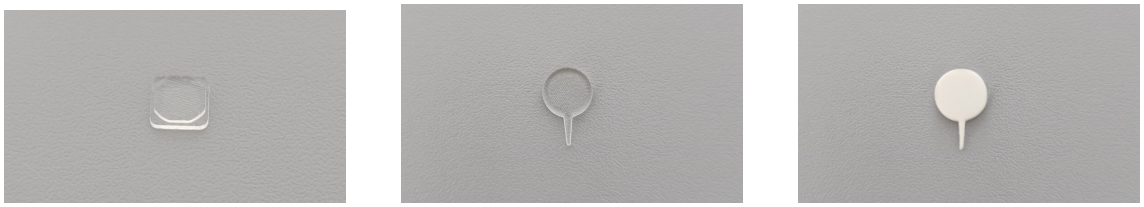

(a) Central chamber tap. (b) Filling channel plug. (c) Lateral outlet plug.

Figure 2.11: 3D-printed plugs for sealing of the microfluidic platform.

2.2.2 PDMS

Material

PDMS stands for Poly(dimethylsiloxane) and it is a silicone elastomer with many applications in microfluidic devices. Chemically speaking, silicones are synthetic polymers made up of repeating units of siloxane (-Si-O), whose bond strength leads to chemical inertness and thermal stability[52]. PDMS shows other interesting properties for microfluidic applications, such as optical transparency, presenting a transmittance up to 90% for visible light wavelength, which allows the direct observation of microflows and the integration of optical components[53]. This material is often used in biomedical research and even considered for medical implants, as it is highly biocompatible and resistant to biodegradation, other than exhibiting high flexibility and elasticity, which is adjustable to specific needs by changing the mixing ratio of elastomer base and curing agent[53;52]. The expanding use of PDMS, especially in manufacturing microfluidic devices, can be connected to the development of Soft Lithography techniques, e.g. replica molding, which allow low-cost, easy fabrication for rapid prototyping[54;53].

Process

The layers of the platform were fabricated in PDMS, by combining SYLGARD™ 184 Silicone Elastomer[55] base and curing agent in a ratio of 10:1 w/w. The action of mixing the two components caused the formation of bubbles in the solution, which was therefore degassed under vacuum before proceeding. This process is visualized in Figure 2.12, with pictures of the initial stage after mixing (2.12a), of the degassing under vacuum (2.12b) and of the result of the operation (2.12c). Once the liquid elastomer was clear of bubbles, it was casted into the previously cleaned and treated master molds, as shown in Figure 2.13. Once again this operation introduced bubbles in the material, therefore the filled molds were put under vacuum to degas. This phase was important to ensure flatness of the surfaces of the PDMS layers, otherwise the bonding to assemble the multi-layer platform would be less effective and thus some leakages at the interfaces could occur. After this final degassing step, the molds with the liquid elastomer were put in the oven at 80°C for 2 hours to achieve PDMS polymerization. The solid results were finally removed from the molds with the help of a cutter, a toothpick and some drops of isopropyl alcohol.

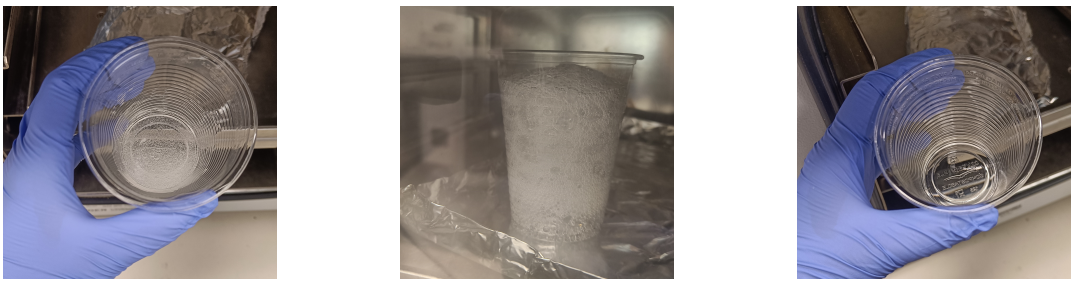

(a) Un-degassed PDMS. (b) PDMS degassing. (c) PDMS after degassing.

Figure 2.12: Process of degassing PDMS under vacuum after mixing base and curing agent.

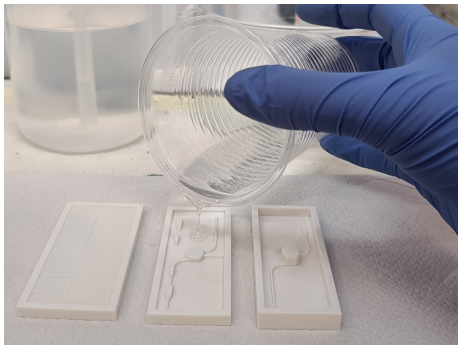

Figure 2.13: PDMS casting into 3D-printed master molds.

2.2.3 Stacking and bonding of PDMS Layers

The microfluidic platform is a multi-layer structure, composed by the three PDMS layers obtained through soft lithography using the master molds in Figure 2.10. These three PDMS sheets were bounded one to the other using two different techniques, in order to compare the results and establish which one was the better option. The fist and simpler bonding technique consisted in spreading a thin film of uncured PDMS on one layer, place the one to be bonded above it and put it in the oven at 80°C for 30 minutes. In this way the PDMS worked as a glue between the layers, sticking them together. The alternative method involved the activation with plasma of the surfaces to be bonded. The used machine was Plasma Asher E2000 manufactured by Bio-Rad, showed in Figure 2.14, the samples were put inside it with the surfaces to be bonded together oriented upward, vacuum was created, then with "GAS1" button a bit of air was let inside and with "RF" button plasma was activated. The surfaces were exposed to plasma for 30 seconds with forward power of 20 W, not too high in order to limit the reflected power. The plasma activation of the surfaces creates dangling bonds that are highly reactive, thus as soon as the layers were extracted from the Plasma Asher they were immediately stuck one over the other, with the membrane in between, and then put on a hot plate at 80°C for 10 minutes to promote covalent bonding. The differences in the results between the two methods are investigated in Section 3.2.1.

Figure 2.14: Plasma Asher E2000 manufactured by Bio-Rad.

2.3 OECTs fabrication

The OECT chips are schematized in Figure 2.15, showing the layout and the expected sizes of the different components. Each chip comprehends three OECT devices, therefore three pairs of source and drain electrodes, connected to the gold pads on the bottom of the chip.

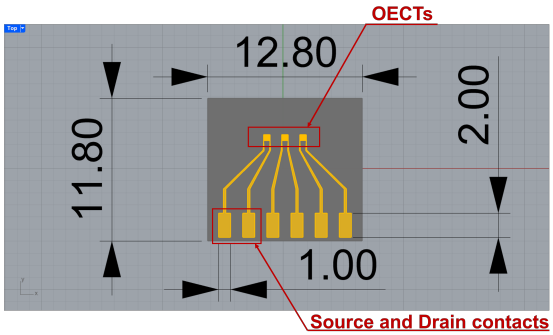

Figure 2.15: CAD representation of an OECT chip, with expected sizes.

The OECT devices used in this work were fabricated in clean room environment through the process summarized in Figure 2.16. The steps can be divided in two lift-off processes: the first one to pattern the gold electrodes (source, drain and gate), the second one to define the passivation layer made of aluminium oxide (Al_2O_3).

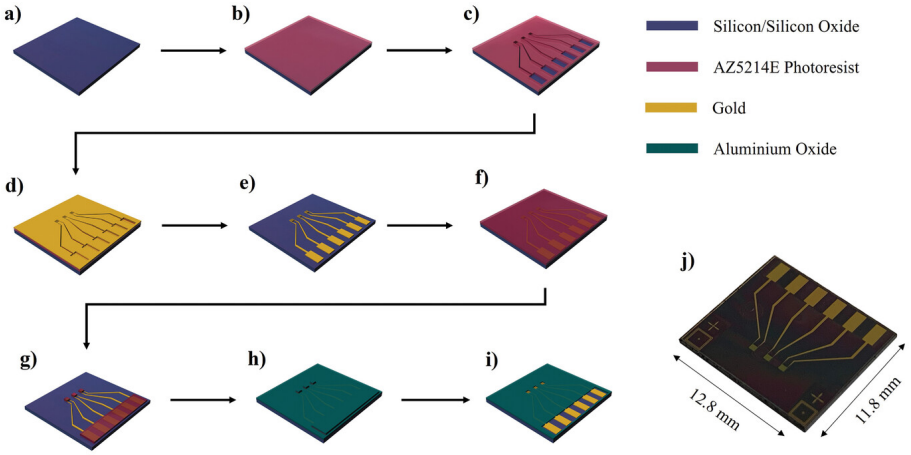

Figure 2.16: Schematic representation of the OECT fabrication steps, consisting in two lift-off steps: a–e) first lift-off used to pattern the gold electrodes; f–i) second lift-off used to define the passivation layer made of aluminium oxide (Al_2O_3). j) Final chip. Reproduced from Segantini et al.[6], licensed under CC BY.

The first lift-off process to pattern the electrodes is represented in Figure 2.16a-e) and consists in the following steps:

- a) The starting point is a 4 inches p-type Silicon wafer covered by 1 µm of thermally grown silicon dioxide (SiO_2).
- b) A layer of AZ 5214E Image Reversal photoresist[56] is spinned on the wafer and soft baked at 110°C for 1 min.

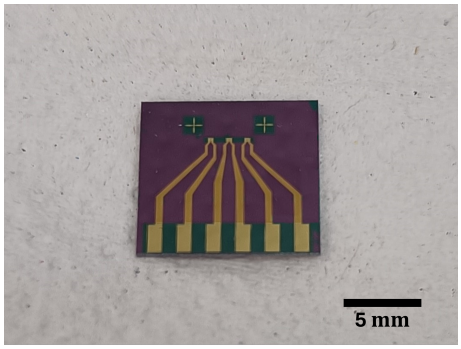

Figure 2.17: Photo of a fabricated OECT chip after the two lift-off processes and dicing, before the PEDOT:PSS deposition.

- c) The photoresist is exposed to UV light and developed, obtaining the source and drain electrodes pattern.
- d) A 100 nm thick layer of gold (Au) is deposited after the e-beam evaporation of a 10 nm Ti adhesion layer.
- e) The first lift-off is performed by immersing the wafer in acetone, removing the photoresist and the excess metal, leaving only the patterned electrodes on the Si/SiO_2 substrate.

The second lift-off is aimed at creating an aluminium oxide passivation layer, it is schematized in Figure 2.16f-i) and here described:

- f) A second layer of AZ 5214E Image Reversal photoresist [56] is spinned on the wafer.
- g) The photoresist is exposed to UV light through a mask defining the passivation layer pattern, then reversal-baked and developed.
- h) A 150 nm thick Al_2O_3 passivation layer is e-beam evaporated on the wafer.
- i) The second lift-off is performed, removing the photoresist and the excess Al_2O_3 and leaving the passivation layer on the Si/SiO_2 substrate, exposing only the channel area and the contact pads.

Lastly, a new layer of photoresist is spinned on the wafer to protect the devices during dicing. Figure 2.16j) shows the final unit, which is obtained by dicing the wafer into single chips. The resulting chip is shown in Figure 2.17, which is however not the complete OECT device yet, as the PEDOT:PSS channel still needs to be deposited. Before being used, the chips are cleaned with three washes of 30 seconds, two in acetone and one in isopropyl alcohol (IPA), then dried with compressed air.

2.3.1 PEDOT:PSS deposition

The channel of the OECT sensor is made of the conductive polymer PEDOT:PSS (Poly(3,4-ethylenedioxythiophene) polystyrene sulfonate), which is not deposited during the clean room fabrication process. The starting point for this phase of the work is the chip in Figure 2.17, cleaned in acetone and isopropyl alcohol (IPA) as described above. From the mentioned picture, it is possible to notice two crosses on the chip, which are alignment marks used during the PEDOT:PSS deposition to correctly place the channel material over the source and drain electrodes of each of the three devices. Before the deposition, the chip was subjected to surface activation by plasma treatment at 50 W forward power for 2 minutes (Plasma Asher E2000 manufactured by Bio-Rad, showed in Figure 2.14), to improve the adhesion of PEDOT:PSS on the substrate. After the deposition, the chips were annealed at 120°C for 45 minutes to improve their conductivity.

Deposition technologies

PEDOT:PSS is an Organic Mixed Ionic-Electronic Conductor (OMIEC) which is available as aqueous dispersion, therefore it can be deposited with solution techniques such as spin coating, inkjet printing or aerosol jet printing[57].

Spin coating is a widely used deposition method consisting in the deposition of the solution on the center of the substrate, which is then rapidly spun to spread the solution by centrifugal force and finally the solvent is evaporated, leaving only the wanted material film. This process is schematically illustrated in Figure 2.18. The thickness of the deposited layer can be controlled by adjusting parameters such as spin speed, acceleration and solution viscosity. However, this technique has some limitations such as a non-uniform distribution of the solution, with a higher thickness in the center[58].

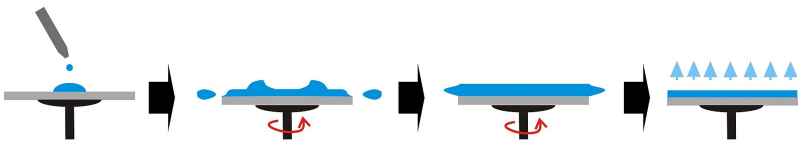

Figure 2.18: Illustration of spin coating deposition process. Image in the public domain[11].

Inkjet and aerosol jet printing are two digital, non-contact deposition techniques working by ejecting droplets of ink onto a substrate, creating a precise pattern. The ink can be constituted either by a solution or a dispersion, depending on the nature of the active material. In inkjet printing, ink drops are ejected from a nozzle of the order of tens of micrometers to be deposited on the substrate. Inkjet printers can be continuous inkjet or drop on demand systems, both schematized in Figure 2.19. In the first case, the droplets formed by a charging electrode are continuously ejected

with a certain frequency and directed by deflection plates towards the substrate or the recycling system, where unused ink is collected and reused. In drop on demand printers, the droplets are created only when needed, usually through the actuation of a piezoelectric element (piezoelectric inkjet printing), but they can also be created thermally, with a rapid heating of a resistor inside the inkjet cartridge which forms a drive bubble (thermal inkjet printing).[59;12]

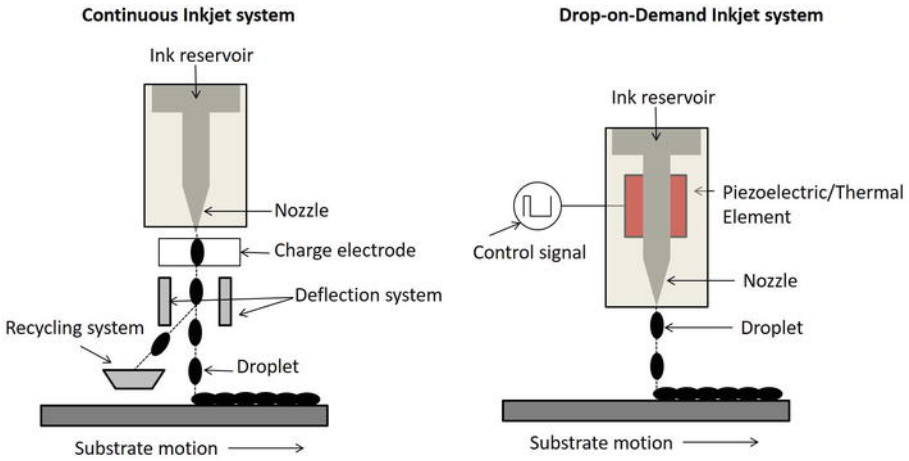

Figure 2.19: Illustration of inkjet printing. Continuous (a) and drop-on-demand (b) inkjet systems. Reproduced from Khan et al.[12], licensed under CC BY.

The working principle of aerosol jet printing is schematized in Figure 2.20 and it consists in the transformation of the ink into an aerosol mist of microdroplets, which is then driven towards the printing nozzle by a sheath gas. The atomizer can be pneumatic or ultrasonic. In the first case the aerosol mist is generated by introducing pressurized air or gas into a sealed chamber containing the ink, while in the second case, the droplets form due to ultrasonic pressure waves. Aerosol jet printing requires some attention in order not to clog the atomizer nozzle, such as a small enough ink particle size. This technique allows high resolution patterns to be printed, with a wide variety of materials.[59;12]

In both the digital printing techniques, the drops are deposited on the substrate, they spread and overlap to form a continuous film after solvent evaporation. The final thickness of the layer depends on parameters such as drop size, drop spacing, ink and substrate properties.[59]

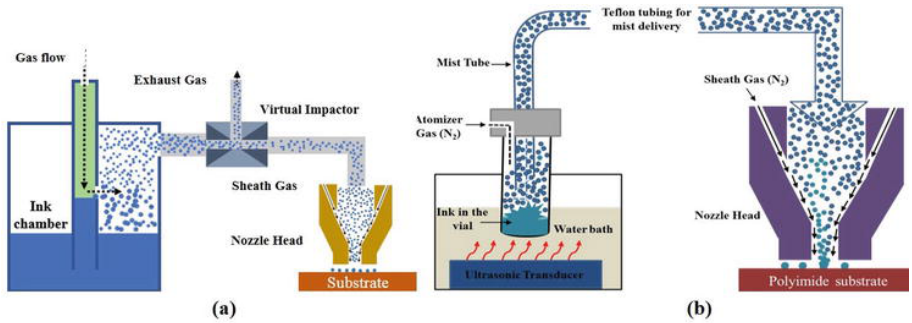

Figure 2.20: Illustration of aerosol jet printing. Pneumatic (a) and ultrasonic (b) aerosol jet printing. Reproduced from Khan et al.[12], licensed under CC BY.

In this work, inkjet printing was selected for the deposition of PEDOT:PSS on the OECT chips, due to the availability of the equipment.

Inkjet printing of PEDOT:PSS

The ink to be printed was prepared starting from an aqueous dispersion of PEDOT:PSS, Clevios® PH1000 by Heraeus[60]. To improve the conductivity of the polymer, the dispersion was mixed with ethylene glycol. Dodecylbenzenesulfonic acid (DBSA) was added as a surfactant to enhance the wetting properties of the ink on the substrate. At this point, the mixture was put in ultrasonic bath for 15 minutes. Lastly, a small amount of (3-glycidoxypropyl)trimethoxysilane (GOPS) was included as a cross-linking agent to improve the stability of the polymer film in polar solvents[57]. The final composition of the ink was the following:

- 76% v/v Clevios® PH1000 PEDOT:PSS dispersion,
- 19% v/v ethylene glycol,
- 4% DBSA,
- 1% GOPS.

The conductive polymer was deposited on the chip through inkjet printing, using a Jetlab 4 DOD by MicroFab Technologies Inc® [13], shown in Figure 2.21. The employed nozzle has a diameter of 80 µm and the printing process is based on the piezoelectric drop on demand (DOD) technology. The formation of a drop is illustrated in Figure 2.22, where the actuation of the piezoelectric element generates a pressure wave which forces a small volume of ink to exit from the nozzle, forming a droplet which is deposited on the substrate. One of the main challenges in inkjet printing is nozzle clogging. To prevent this issue, the nozzle was cleaned before and after the process by suctioning filtered deionized water through it, effectively removing any residual particles.

The Jetlab 4 DOD setup for printing is shown in Figure 2.23, with highlights on the main elements, such as the ink reservoir, the electrical connections for the piezoelectric element, the printing head, the ink channel and the back-pressure channel. This last component is connected to a pump which controls the pressure to regulate the ink flow towards the nozzle. A positive back-pressure pushes the ink in a channel towards the printing head, while a negative back-pressure pulls the ink away from the nozzle, preventing unwanted dripping. A slightly negative back-pressure was set during the printing of PEDOT:PSS to obtain stable drop formation.

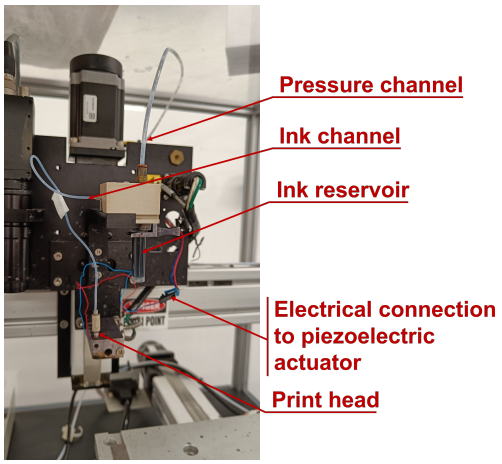

Figure 2.23: Jetlab 4 DOD setup for printing, with labels indicating the main components.

The main printing parameters used for the deposition of PEDOT:PSS on the OECT

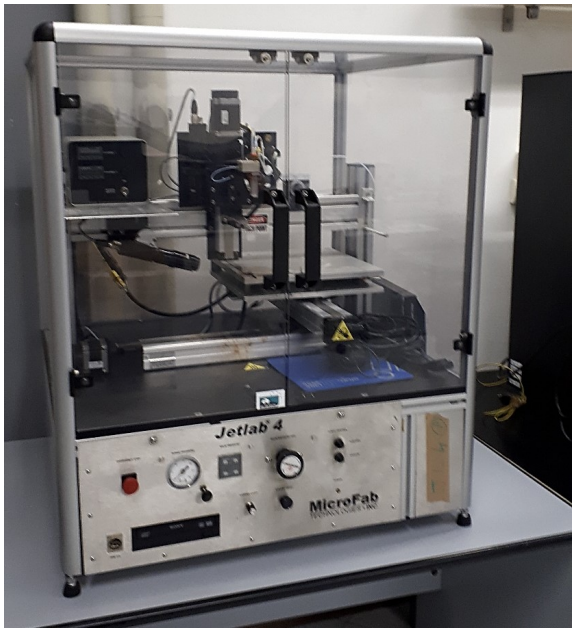

Figure 2.21: Jetlab 4 DOD by MicroFab Technologies Inc.[13].[14]

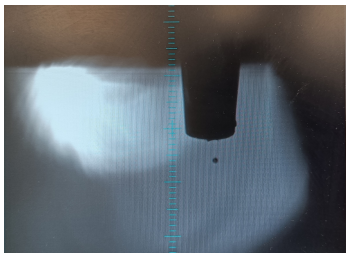

Figure 2.22: Drop formation in inkjet printing. Extended figures in[15].

chips are summarized in Table 2.2. The drop spacing was varied to obtain different channel thicknesses, while the other parameters were kept constant. The channel length and width are defined by the geometry of the source and drain electrodes on the chip, therefore they are not influenced by the printing parameters.

Parameter	**Value**
Rise time 1	3 µs
Rise time 2	3 µs
Dwell time	40 µs
Fall time	6 µs
Echo time	40 µs
Dwell voltage	-50 V
Echo voltage	50 V
Frequency	1000 Hz
Spot margin	1 µm
Spot spacing	**80, 100 and 120 µm**
Fly velocity	25 mm/s

Table 2.2: Main parameters used for the inkjet printing of PEDOT:PSS on the OECT chips.

2.4 Gate electrodes fabrication

In order to be able to use the OECT devices as transistors they need to be paired with gate electrodes, which were fabricated in clean room environment. The scope of this project is to use the OECTs as sensors for biological applications, therefore the gate material must be biocompatible and stable in aqueous solutions. For this reason and with the perspective to functionalize the electrode surface, gold was chosen as the gate electrode material due to its well-known biocompatibility and chemical stability. The fabrication process of the gold gates was equal to the one used for the OECT electrodes, in particular the first steps for the first lift-off (Figure 2.16a-d)), consisting in lithography with image reversal photoresist and deposition of a thin Ti adhesion layer followed by 100 nm thick Au layer. An additional step of deposition of photoresist was executed to protect the electrodes during dicing. The gold gate resulting from the process after dicing the wafer is shown in Figure 2.24a, with dimensions of 7.8 mm x 11.8 mm. The chips were washed for 30 seconds twice in acetone and once in isopropyl alcohol, before being integrated into the platform. Figure 2.24 shows the gate before and after the cleaning step, with noticeable differences in the appearance of the gold surface. The showed pattern of the gates comprehends a smaller rectangle to be put in contact with the ionic solution through the microfluidic channel, while the bigger rectangle on the edge of the chip is used for electrical connection to the measuring unit.

In order to make a comparison with different gate materials (Section 3.3), silver gates were obtained by sputtering Ag on top of the gold gates.

(a) Gate electrode after fabrication process, before cleaning.

(b) Gate electrode after cleaning in acetone and isopropyl alcohol.

Figure 2.24: Gate electrode resulting from the fabrication process, of size 7.8 mm x 11.8 mm.

2.4.1 Gate functionalization

In order to detect specific analytes, the gate electrodes need to be functionalized with a suitable receptor layer. A common method to functionalize gold surfaces is through the formation of a self-assembled monolayer (SAM), which provides a stable and organized platform for immobilizing biomolecules. The structure of a generic SAM is schematically represented in Figure 2.25, composed of three main components: a head group that binds to the surface, a tail group that extends away from the surface, and a terminal functional group that can be used for further modifica-

tion or interaction with target molecules. SAMs allow to immobilize biomolecules with high stability, due to the covalent nature of the bonds. They can be formed both with small molecules (such as thiols) and polymers. The SAM molecules must contain functional groups that can link to the surface and be able to self-assemble with high density and uniformity, creating a well-ordered, unidirectional monolayer. The formation of a 2D ordered structure depends on different types of interactions, including surface-adsorbate ones, intramolecular (torsion, bond stretches), electrostatic and van der Waals.[16]

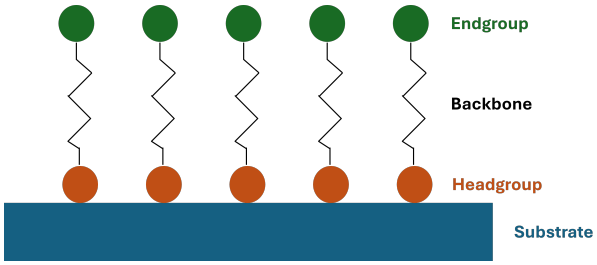

Figure 2.25: Schematic representation of the structure of a generic self-assembled monolayer (SAM). Adapted from[16].

Gold is a widely used substrate for SAM formation due to its properties such as chemical inertness, biocompatibility and ease of functionalization. Its applications cover various fields, including microfabrication, gas sensing and biosensing, which is the focus of this work. The formation of a SAM on gold is typically achieved using alkanethiols, which spontaneously assemble into an ordered structure due to the strong affinity between the thiol group and the gold surface. The SAM provides a well-defined interface for further functionalization with biomolecules such as antibodies, aptamers, or peptides.[16]

In this work, the SAM on the gold gate electrodes was obtained using the dipping technique, which consists in the immersion of the substrate into a solution containing the desired molecules. The process to form a SAM on the gold gate electrodes started with a cleaning step in acetone bath for 10 minutes, then rinsed with isopropyl alcohol and dried with nitrogen flow. Afterwards, the electrodes were incubated for 1 hour in a thiol solution of 10 mM 3-mercaptopropionic acid (3-MPA) dissolved in ethanol. 3-MPA is a commonly used alkanethiol for SAM formation on gold surfaces, featuring a thiol group (-SH) that binds to the gold surface and a carboxyl group (-COOH) that can be used for further functionalization. After the incubation, the electrodes were washed twice in ethanol and once in ultra pure water to remove unbound molecules and dried with nitrogen gas. After forming the self-assembled monolayer of 3-MPA, the carboxyl groups on the electrode surface need to be activated to enable covalent coupling with biomolecules containing amine groups, such as antibodies. This activation was achieved through carbodiimide chemistry. Initially, the electrodes were incubated for 15 minutes in a 50 mM solution of 2-(N-morpholino)ethanesulfonic acid (MES) with 0.9% NaCl (MES buffer), which provided the acidic conditions required for the reaction. Subsequently, the samples were incubated for 15 minutes in MES buffer containing 4 mM EDC (1-ethyl-3-(3-dimethylaminopropyl)carbodiimide) and 10 mM Sulfo-NHS (N-hydroxysulfosuccinimide). In this step, EDC reacts with the carboxyl groups to form an O-acylisourea intermediate, which is highly unstable. Sulfo-NHS stabilizes

this intermediate by converting it into an NHS ester, a reactive species that can efficiently bind to primary amines of proteins. After activation, the electrodes were rinsed three times with PBS (Phosphate Buffered Saline), 5 minutes each on an orbital shaker to remove excess reagents and then dried under a nitrogen stream.

Finally, the gold gates were functionalized by decorating the SAM with anti-Ang2 antibodies, for the detection of Angiopoietin-2 (Ang2), a common choice as cancer biomarke. Ang2 is a protein involved in angiogenesis, the formation of new blood vessels, and its overexpression has been linked to tumor growth and metastasis in various cancers. In the specific case of this project, the detection of Ang2 was used as a proof-of-concept for the biosensing capabilities of the OECT platform, since Ang2 is a well-studied biomarker with established detection methods. The electrodes were incubated overnight at 4 °C in an 80 µm PBS solution with 5 µg/mL of anti-Ang2 antibodies, then they were subjected to three washing steps in 0.05% (v/v) Tween®20-supplemented PBS (PBS-tween) on an orbital shaker for 5 minutes to remove unbound antibodies. Finally, the electrodes were dried with nitrogen gas and integrated in the platform for sensing tests.

2.5 Microfluidic leakage tests

Microfluidic leakage tests were performed in order to verify the sealing of the channels in the fabricated multi-layer platform. A syringe pump (model 33 from Harvard Apparatus[17]) was used to inject a PBS solution in water into the microfluidic channels at a constant flow rate of 30 µL/min. The liquid was colored with a food dye to allow visual inspection of any potential leakage points. The setup is shown in Figure 2.26.

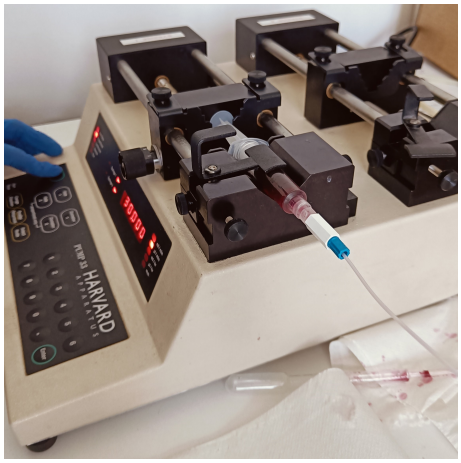

Figure 2.26: Syringe setup used for microfluidic leakage tests, with Syringe Pump model 33 from Harvard Apparatus[17].

2.6 Electrical Measurements

The OECT sensors were electrically characterized to evaluate their performance in the developed multi-layer microfluidic platform. The measurements were performed using a Keysight B2912A Precision Source/Measure Unit (SMU), shown in Figure 2.27, which was controlled through Quick IV Measurement Software. The chips with the OECT devices and the gates were placed in the microfluidic platform, which was filled with 1x PBS solution in water as the electrolyte between the gate electrode and the OECT channel. The electrical characterization involved measuring both the output and transfer characteristics of the OECTs, presented in Section 3.3.

Figure 2.27: Keysight B2912A Precision Source/Measure Unit (SMU) [18].

2.6.1 Measurement Setup

The setup for the electrical measurements included micromanipulators to accurately contact the gold pads on the chips, as shown in Figure 2.28. These micromanipulators were connected to the SMU to apply the necessary voltages to the source, drain and gate electrode and measure the resulting currents in the OECT devices. The different electrodes are indicated in Figure 2.28, source and drain are directly connected to the channel of the OECT device while the gate acts on it through the electrolyte solution. Since the OECTs are symmetric, source and drain can be interchanged without affecting the measurements. Channel 1 of the SMU is connected to source and drain, applying a drain-source voltage (V_{DS}) and measuring the drain current (I_D), while Channel 2 is connected to the gate electrode, applying a gate voltage (V_G) and measuring the gate current (I_G).

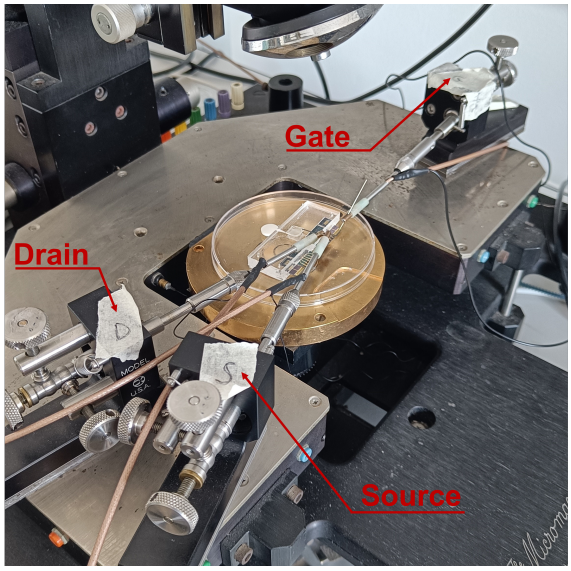

Figure 2.28: Setup for electrical measurement to characterize OECT devices, with the use of micromanipulators for contacting the gold pads on the chips.

2.6.2 Settings

The electrical measurements were conducted using the Quick IV Measurement Software, which allows for precise control of the voltage sweeps and current measurements. For the output characteristics, the drain-source voltage (V_{DS}) was swept from 0 V to -0.6 V in steps of -0.02 V, while the gate voltage (V_G) was held constant at different values ranging from -0.2 V to 0.6 V in steps of 0.1 V, as shown in Figure 2.29. For the transfer characteristics, V_G was swept from -0.2 V to 0.8 V and backwards in steps of 0.025 V for five repetitions, while V_{DS} was held constant at -0.4 V, as depicted in Figure 2.30.

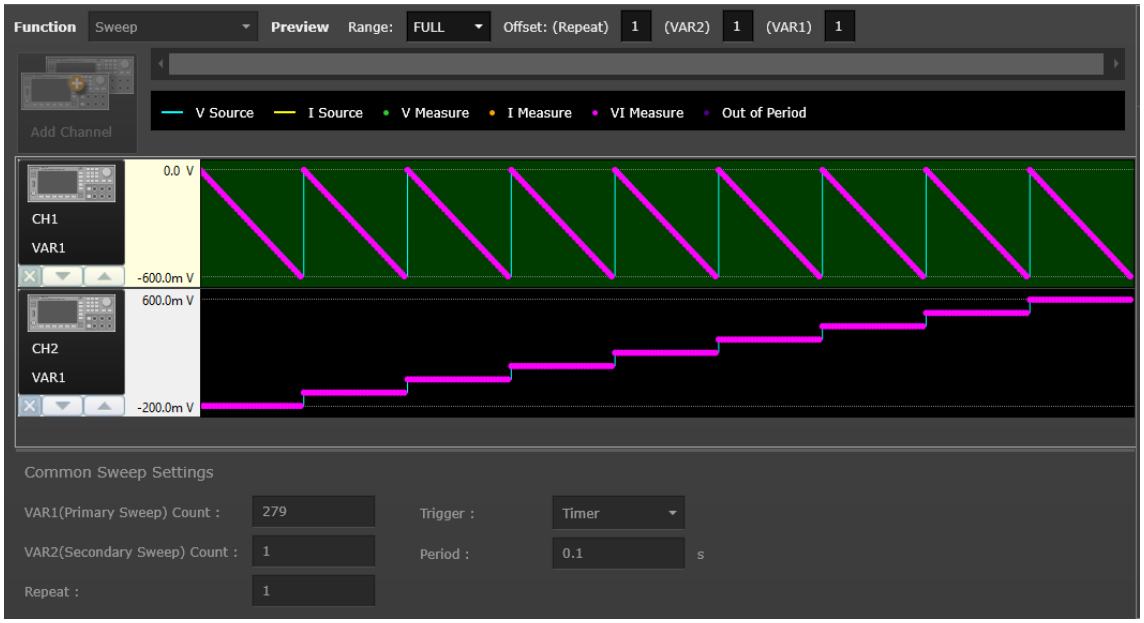

Figure 2.29: Measurement settings on Quick IV Measurement Software for the output characteristics of the devices.

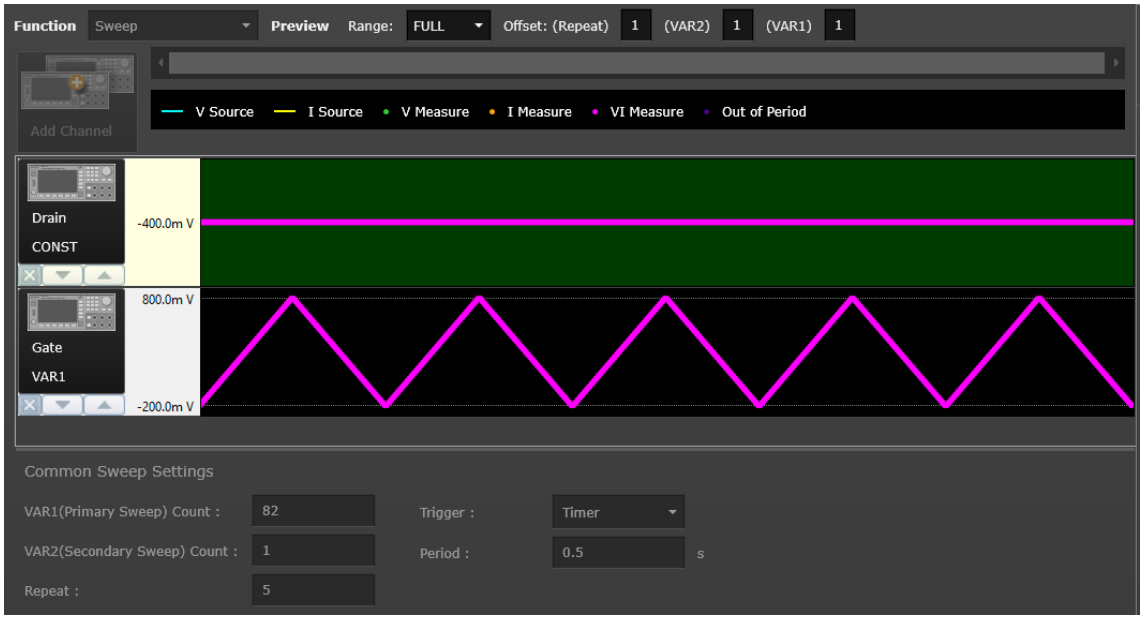

Figure 2.30: Measurement settings on Quick IV Measurement Software for the transfer characteristics of the devices.

Chapter 3

Results

3.1 Device fabrication

In this section the results of the fabrication processes are presented, including the multi-layer microfluidic platform and the PEDOT:PSS deposition on the OECT chips. For what concerns the PDMS platform fabrication, all the different versions (0, 1 and 2) of the device described in Section 2.1 are shown, highlighting the reasons behind some design modifications. Regarding the PEDOT:PSS deposition, microscope images of the deposited ink with different drop spacings are reported and discussed.

3.1.1 Microfluidic platform

The assembled multi-layer microfluidic platforms with the two different membranes are shown for all three device versions. Version 0 features a symmetric structure for initial testing, while versions 1 and 2 include updated designs for the thin PC membrane and the thicker silk membrane, integrating OECT chips and gold gates as detailed in Section 2.1.

Version 0

First of all the two different membranes were integrated in the version 0 of the multi-layer microfluidic platform, as shown in Figure 3.1, in order to test the fabrication process and the bonding between the PDMS layers and the membranes. The device structure is exactly the same in both cases, it is perfectly symmetric, composed by two layers with microfluidic channels in PDMS, separated by the membrane in the middle. As it can be noticed by comparing the two pictures, the thicker silk membrane produced by KLISBio (Figure 3.1b) causes a non-uniform bonding between the two PDMS layers, with a visible bubble around the membrane perimeter, due to the difficulty of achieving a good contact between the two layers close to the thick membrane edges. On the other hand, the thin PC membrane produced by Oxyphen (Figure 3.1a) allows a uniform bonding between the two PDMS layers, without any visible imperfections. This issue was one of the main reasons for redesigning the microfluidic platform for the integration of KLISBio membrane, in order to avoid having it sandwiched between two PDMS layers, as explained in Section 2.1, introducing in particular an excavation in the top PDMS layer to accommodate the thicker membrane in version 2 of the platform.

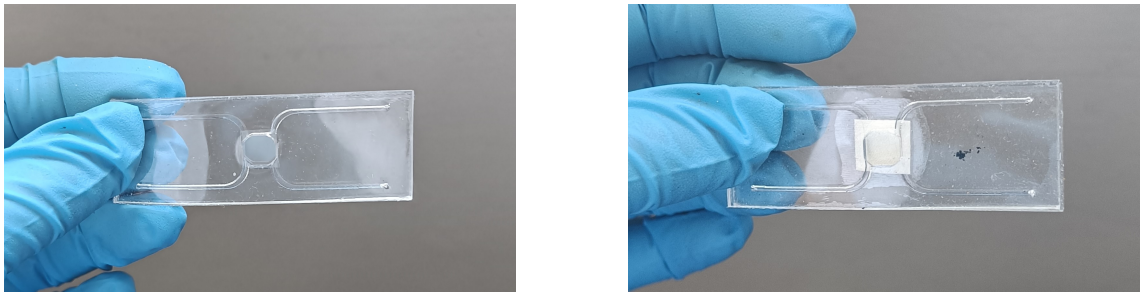

(a) With Oxyphen thin PC membrane. (b) With KLISBio thick silk membrane.

Figure 3.1: Multi-layer microfluidic platform version 0, assembled with the two different membranes through plasma bonding.

Version 1 and 2

The assembled multi-layer microfluidic platforms are shown in Figures 3.2 and 3.3. Figure 3.2 shows the platform version 1, assembled with the Oxyphen thin PC membrane, which is transparent and therefore it is not very visible in the pictures. From Figure 3.2a it is possible to see the channels shape in the PDMS layers, with inlets and outlets in the top layer and the filling channel on the side, closed with a custom 3D-printed plug with decreasing cross section. Figure 3.2a allows to see also the alignment of the two chips inside the platform and the shape of the little chambers connecting OECTs to the microfluidic channels, which are visible also from the frontal point of view in Figure 3.2b, where their vertical extension is clearer. The platform in Figure 3.2 is the final version for the commercial membrane, with the PDMS closing layer extending below the chips, to provide better mechanical support during measurements. Figure 3.3 shows the platform version 2, assembled with the KLISBio thicker silk membrane. In this version, the channels are extended to the lateral sides of the PDMS structure in order to have easier flow towards the outlets, while the inlets remain on the top layer. The lateral holes for the outlets require other two 3D-printed plugs, similar to the one used for the filling channel, but with rectangular section. Figure 3.3a shows the platform without the extended PDMS closing layer below the chips, while Figure 3.3b shows the version with the support layer. The latter is the final version for the KLISBio membrane, as it provides better mechanical stability during measurements. The reason why it was necessary to extend the PDMS closing layer below the chips is represented in Figure 3.4, which shows the platform in the measurement setup with micromanipulators. Figure 3.4a presents the device in the measurement setup before contact with the micromanipulator probes, without the PDMS support layer below the chips. In this condition, when the probes press on the electrodes surface (Figure 3.4b), the chips bend downwards due to the lack of support, causing unreliable contact and possible leakages or damage to the device, even tilting the whole platform if too much pressure is applied, as in this case. Due to these issues, the extended PDMS closing layer below the chips was added, as shown in Figure 3.4c, which provides a stable support for the chips during measurements, avoiding bending and tilting of the platform.

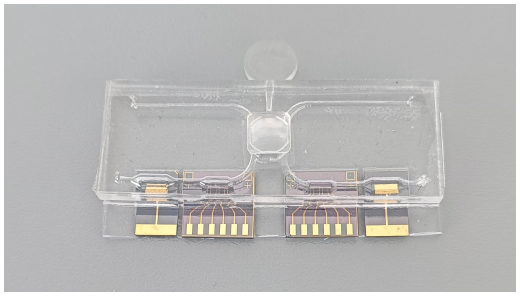

(a) Perspective view.

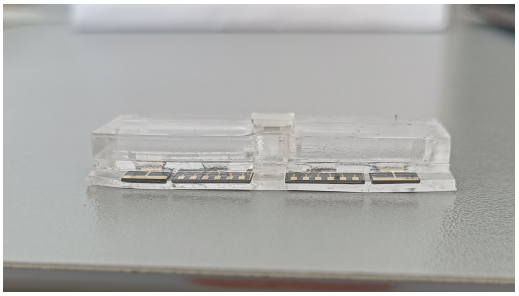

(b) Front view

Figure 3.2: Multi-layer microfluidic platform assembled with Oxyphen thin PC membrane.

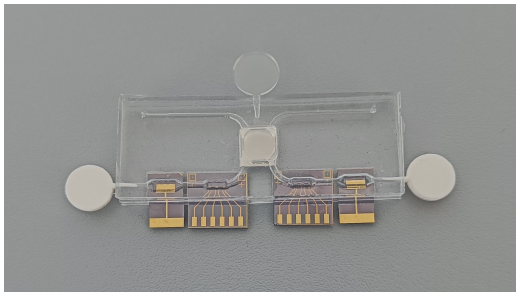

(a) Initial version of closing layer.

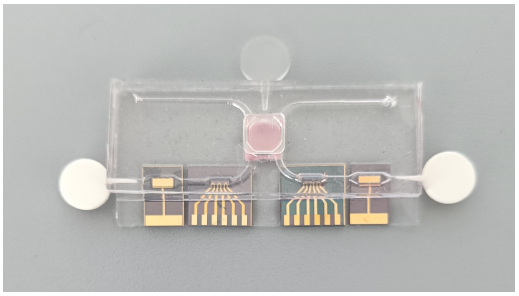

(b) With extended PDMS closing layer.

Figure 3.3: Multi-layer microfluidic platform assembled with KLISBio thick silk membrane, with and without the extended closing layer below the chips.

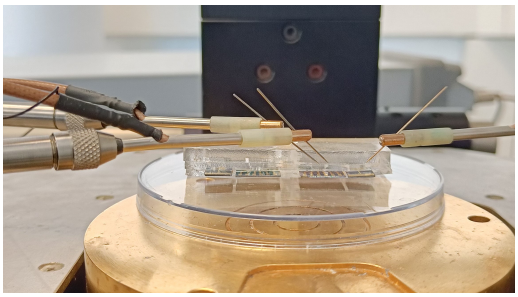

(a) Before contact, without support.

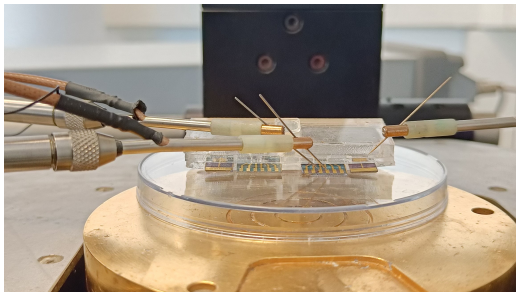

(b) During contact, without support.

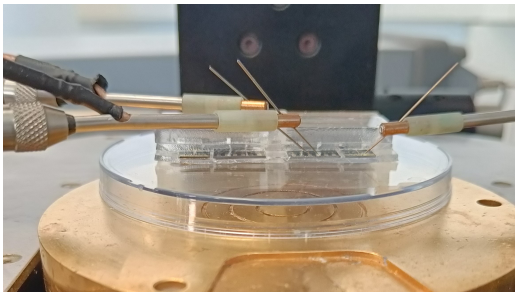

(c) During contact, with support.

Figure 3.4: Multi-layer microfluidic platform in measurement setup with micromanipulators, with and without the extended closing layer below the chips.

3.1.2 OECT chip with deposited PEDOT:PSS

As explained in Section 2.3.1, different spacings between the ink drops were tested during the inkjet deposition of PEDOT:PSS on the OECT chips. A Leika Microsystems microscope was used to get images of the deposited PEDOT:PSS with different spacings, shown in Figure 3.5. All three images show a uniform deposition of the ink, with no visible gaps between the drops, demonstrating the effectiveness of the inkjet deposition process for creating a continuous PEDOT:PSS layer on the OECT chips. However, the spacing affects the thickness of the deposited layer, with smaller spacings resulting in thicker layers, causing less defined edges of the printed pattern. This effect is visible by comparing Figures 3.5a, 3.5b and 3.5c, where the edges of the PEDOT:PSS layer become progressively sharper as the spacing increases from 80 µm to 120 µm, while the thickness decreased, which can be noticed by the color difference of the deposited layer and the contrast with respect to the substrate.

In general, an higher thickness of the PEDOT:PSS layer can lead to better electrical conductivity and improved performance of the OECTs, but it can also cause issues such as smaller ON/OFF current ratio. Therefore, the choice of spacing should be optimized based on the specific requirements of the application.

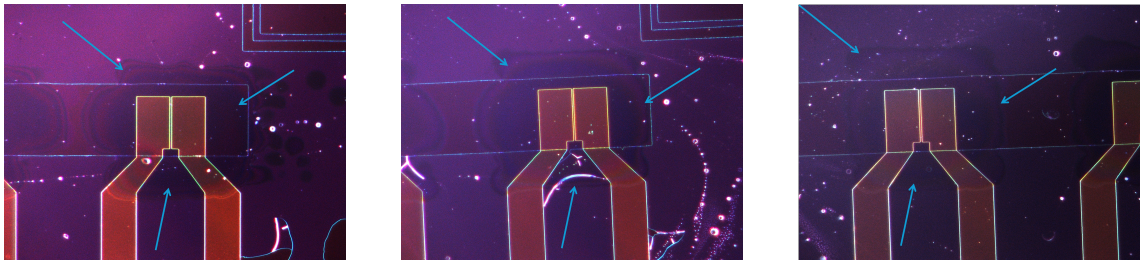

(a) Spacing: 80 µm (b) Spacing: 100 µm (c) Spacing: 120 µm

Figure 3.5: Inkjet deposited PEDOT:PSS on the OECTs chips, with different spacing between the deposited ink drops, highlighted by the blue arrows. Images taken with Leica Microsystems microscope.

3.2 Microfluidic leakage tests

The microfluidic leakage tests were performed on the multi-layer platforms with both Oxyphen and KLISBio membranes, assembled with different bonding techniques. The aim of these tests was to evaluate the sealing quality of the microfluidic channels and to identify any potential leakage points. The platforms were observed for any signs of leakage at the interfaces between layers, at the taps, around the membrane and through the membrane itself. The platforms used in this tests were the ones fabricated before the implementation of the extension of the closing layer. This extension was added later as mechanical support for the chips, but it did not affect the sealing of the microfluidic channels, therefore the results of the leakage tests performed on these platforms are still valid.

3.2.1 Leakage tests with device version 1, Oxyphen membrane

In this section the results of the leakage tests performed on version 1 of the multi-layer microfluidic platforms, assembled with Oxyphen membrane, are explored. Two different bonding techniques were used: adhesive bonding with PDMS and plasma bonding.

Bonding with PDMS

A first device closed with PDMS adhesive bonding and with a top plug of thickness 0.5 mm showed leakage issues both at the front side and on the top and side of the platform, as shown in Figure 3.6. The leakage at the front side (Figure 3.6a) was due to an incomplete sealing between the bottom and closing layers, causing the chip to be partly free to move and therefore not sealing the connection with the microfluidic channel. The leakage on the opposite side (Figure 3.6b, circled) came from a non-uniform bonding between the top and bottom layers, as the liquid dripped at the interface between the two layers. On the other hand the leakage on the top (Figure 3.6b) is simply due to a non-perfect sealing of the tap, which is the reason why a thicker one of 0.7 mm was fabricated and used in the following tests.

A second device assembled with PDMS adhesive bonding and with a top plug of thickness 0.7 mm showed no leakage issues, as shown in Figure 3.7. Both the front side (Figure 3.7a) and the top view (Figure 3.7b) showed no signs of leakage, demonstrating that the thicker tap improved the sealing of the platform and that the PDMS adhesive bonding technique can be effective for assembling multi-layer microfluidic platforms with Oxyphen membrane.

Plasma bonding

Figure 3.8 reports the results of the microfluidic tests performed on the multi-layer membrane with PC commercial membrane, assembled through the plasma activation of the surfaces an then heating, with a top plug of thickness 0.7 mm. Both the front side (Figure 3.8a) and the top view (Figure 3.8b) showed no signs of leakage, validating this bonding technique for the assembly of multi-layer microfluidic platforms with the thin membrane. Despite the demonstration that both bonding methods allow good sealing of the microfluidic channels, the plasma bonding was preferred for the fabrication of the final devices due to its higher reproducibility and the absence of any risk that the adhesive PDMS layer could enter the microfluidic channels during assembly.

In order to demonstrate the effectiveness of the membrane in separating the two microfluidic channels, a test was performed in which only one channel was filled with the dyed PBS solution, while the other channel remained empty. Figure 3.9 shows the top view of the platform after the test, proving that the dyed solution remained confined to the filled channel, with no visible leakage or cross-contamination to the adjacent empty channel. This result confirms the integrity and functionality of the Oxyphen membrane in maintaining separation between the two microfluidic channels, allowing co-culture applications.

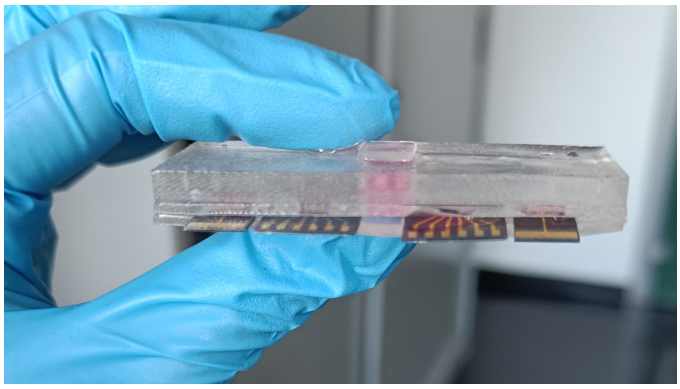

(a) Leakage at the front side.

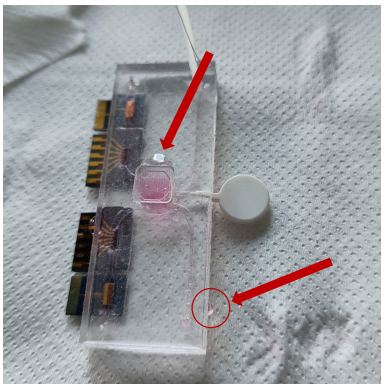

(b) Leakage on the top and side.

Figure 3.6: Leakage tests on multi-layer microfluidic platform assembled with thin PC membrane through adhesive bonding, with 0.5 mm tap.

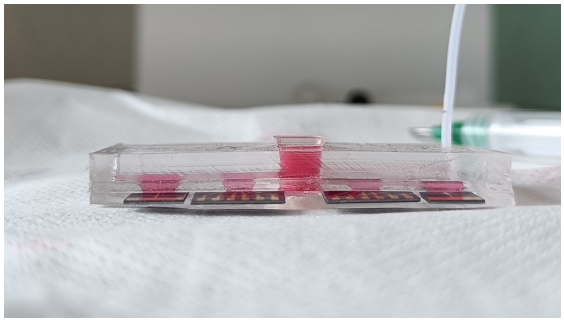

(a) Front side view.

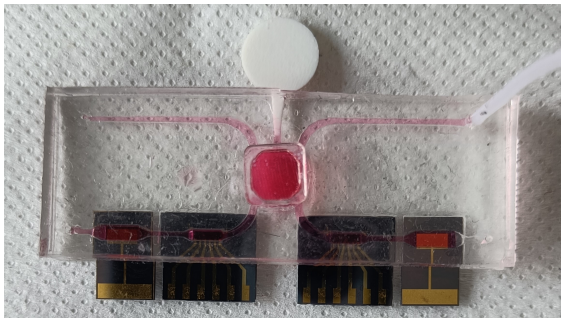

(b) Top view.

Figure 3.7: Leakage tests on multi-layer microfluidic platform assembled with thin PC membrane through adhesive bonding, with 0.7 mm tap.

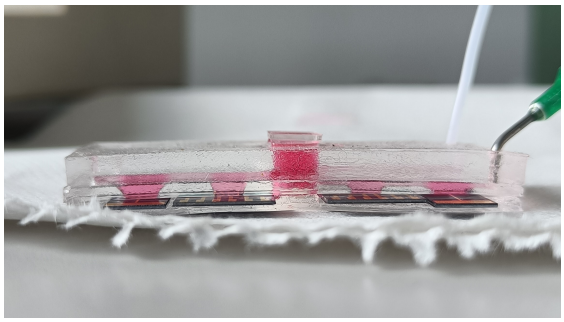

(a) Front side view.

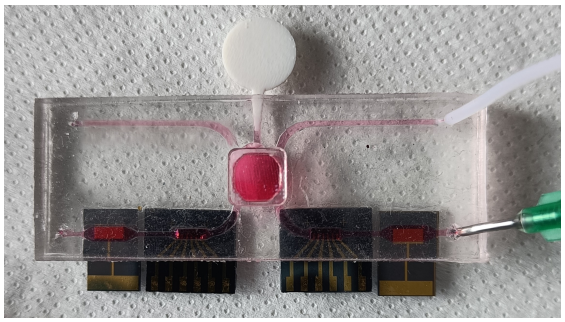

(b) Top view.

Figure 3.8: Leakage tests on multi-layer microfluidic platform assembled with thin PC membrane through plasma bonding, with 0.7 mm tap.

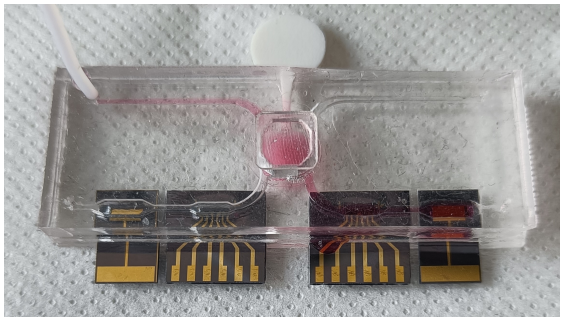

Figure 3.9: Microfluidic test showing the separation of the two channels by the Oxyphen membrane.

3.2.2 Leakage tests with device version 2, KLISBio membrane

The tests on the microfluidic platform with the silk membrane (version 2) were performed on devices closed with plasma bonding only, as it was judged more reliable than the adhesive bonding with PDMS, based on the results obtained with the Oxyphen membrane. The sealing of the channels was obtained to be good, as shown in Figure 3.10a, where no leakage between layers or from the taps was observed. Figure 3.10b shows the same device without the lateral plugs, to better visualize the channels. The performed tests demonstrated the effectiveness of the plasma bonding technique and of the design of the multi-layer platform for the thicker membrane and the lateral plugs. In particular, the excavation in the top layer to accommodate the thicker membrane proved to be functional in ensuring a uniform bonding between the layers, contrarily to what happened with version 0 of the device in Figure 3.1b.

Limitations of the KLISBio membrane

Despite the good sealing performance of the microfluidic platform, the device incorporating the KLISBio membrane presented some issues directly related to the membrane itself. As shown in Figure 3.11a, although there were no leakages from the channels, the two sections of the central chamber, supposed to be separated by the membrane, were not properly isolated. The arrows in the figure highlight how the segment of the channel between the central chamber and the outlet was being filled, even though the liquid entering from the inlet had not yet reached the membrane. Meanwhile, the channel on the opposite layer was filled up to the central chamber, but not beyond it toward the outlet. This behavior indicates that the liquid passed through the membrane and reached the other side, demonstrating that the two sections of the central chamber are not effectively separated. Such a condition could interfere with the cell culture process. Another encountered issue was the bending of the membrane, as shown in Figure 3.11b. This bending is likely due to the absorption of liquid by the membrane, which causes it to deform and potentially come into contact with the opposite layer. This deformation could lead to not optimal support for the model and unintended interactions between the two layers, further complicating the cell culture environment.

Addressing these limitations would be crucial for ensuring the functionality and reliability of the microfluidic platform for biological applications. One potential

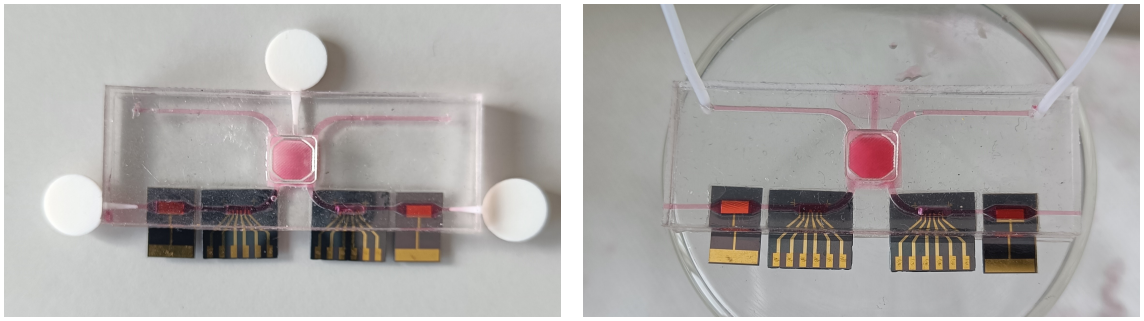

(a) With lateral plugs. (b) Without lateral plugs.

Figure 3.10: Leakage tests on multi-layer microfluidic platform assembled with KLISBio membrane through plasma bonding, with 0.7 mm top plug, with and without lateral taps to better show the channels.

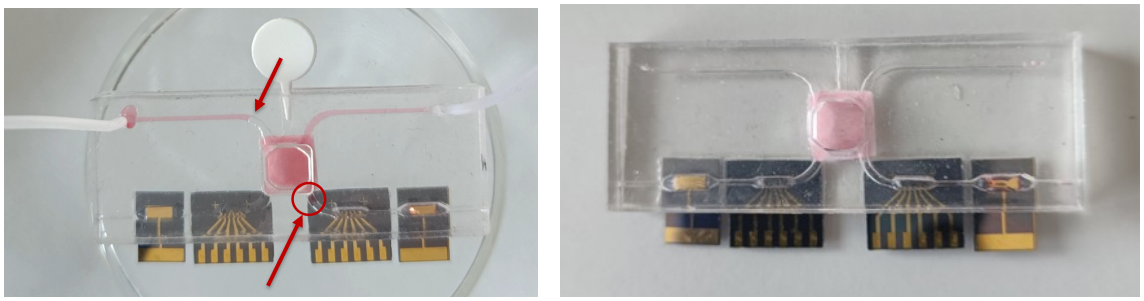

(a) Leakage through the membrane. (b) Bending of the membrane.

Figure 3.11: Observed problems with KLISBio membrane.

solution to mitigate the leakage through the membrane could involve applying a coating to the membrane to enhance its barrier properties. However, preliminary attempts using a gelatin coating did not resolve the issue. A more effective approach might involve hydrophobizing the membrane to reduce its permeability to aqueous solutions. Additionally, incorporating a central support pillar within the membrane could help limit bending by providing structural reinforcement.

3.3 OECTs electrical characterization

As explained in Section 2.6, the OECT devices were electrically characterized with an electrolyte solution of 1x PBS (in water). Measurements were performed on three inkjet-printed chips, each produced with a different drop spacing as reported in Table 2.2 (80, 100, and 120 µm), resulting in variations in the deposited PEDOT:PSS. A representative device from each chip was imaged under the microscope, as shown earlier in Figure 3.5. The characterization involved measuring both the output and transfer characteristics of the OECTs, which are presented in the following. The reported curves correspond to one of the devices on each chip, selected as illustrative of the overall behavior observed across multiple devices, all the measured characteristics are reported in Appendix 4.

3.3.1 Output characteristics

The output characteristics were obtained by sweeping the drain-source voltage (V_{DS}) from 0 to -0.6 V in steps of 0.02 V, while keeping the gate-source voltage (V_{GS}) constant at values ranging from -0.2 V to 0.6 V in steps of 0.1 V (Figure 2.29). The output characteristics for the three different drop spacings are shown in Figure 3.12, with different colors for different V_{GS} values. The plots are reported all in the same axis range to facilitate comparison between the different devices. At a first glance, it can be observed that the device with the smallest drop spacing (80 µm) exhibits the highest drain current (I_{DS}) values, while the device with the largest drop spacing (120 µm) shows the lowest I_{DS} values. This trend is consistent with the expectation that a smaller drop spacing leads to a thicker PEDOT:PSS layer, which in turn results in lower channel resistance and higher current flow. Table 3.1 reports the ON current values at $V_{DS} = -0.6$ V for the maximum and minimum V_{GS} applied for each device, confirming the trend of decreasing ON current with increasing drop spacing.

Figure 3.13 compares the output characteristics of the OECT with 120 µm drop spacing using gold and silver gate electrodes. The characteristics of the OECT with the gold gate is the same as in Figure 3.12c, but with a different range on the y-axis to better visualize the differences between the two gate materials. It can be observed that even if the ON current is lower with respect to Figure 3.13a, the device with the silver gate exhibits overall a better performance (Figure 3.13b), with a clear improvement in terms of the action of the gate on the channel current. The test with the silver gate was performed in order to investigate the effect of different gate materials on the OECT performance. However, for the purpose of this work, which focuses on biosensing applications, gold gates will be primarily used due to their biocompatibility and suitability for functionalization with biomolecules.

Drop Spacing (µm)	I_{ON} at $V_{GS} = -0.2$ V (mA)	I_{ON} at $V_{GS} = 0.6$ V (mA)
80	-25.65	-14.50
100	-23.38	-12.10
120	-20.31	-8.58

Table 3.1: ON current values at $V_{DS} = -0.6$ V for different drop spacings and gate voltages.

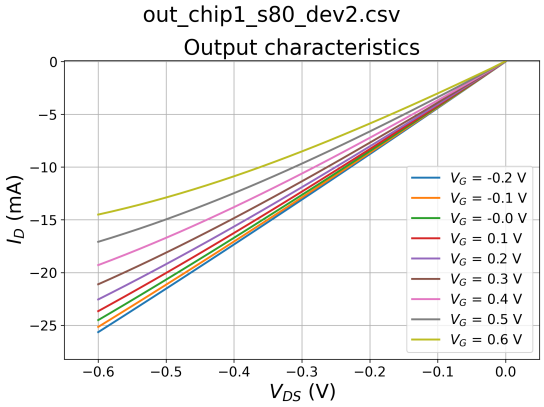

(a) Drop spacing: 80 µm

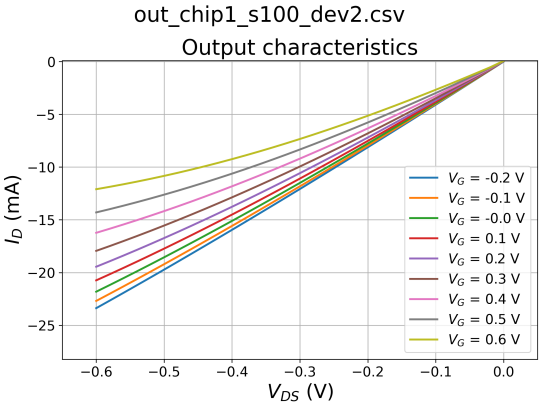

(b) Drop spacing: 100 µm

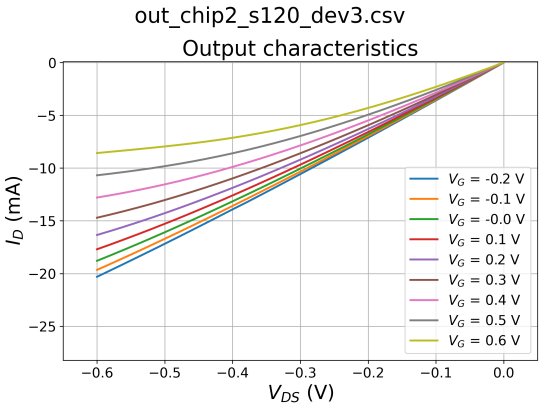

(c) Drop spacing: 120 µm

Figure 3.12: Output characteristics of OECTs with different drop spacings: 80 µm, 100 µm and 120 µm.

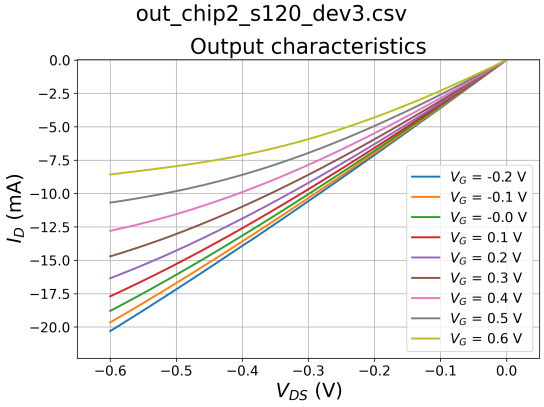

(a) With gold gate.

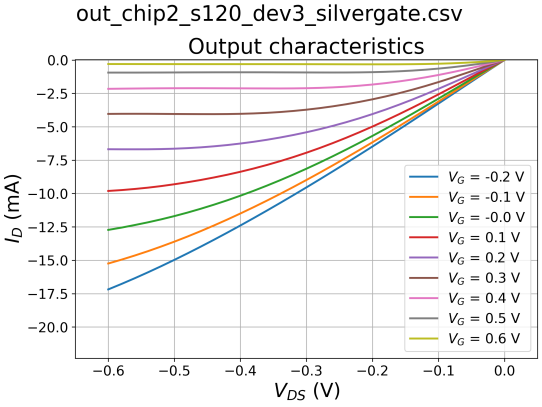

(b) With silver gate.

Figure 3.13: Comparison of output characteristics of OECT with 120 µm drop spacing using gold and silver gate electrodes.

3.3.2 Transfer characteristics

The transfer characteristics were obtained by sweeping the gate-source voltage (V_{GS}) from -0.2 V to 0.8 V in steps of 0.025 V, while keeping the drain-source voltage (V_{DS}) constant at -0.4 V (Figure 2.30). The transfer characteristics for the three different drop spacings are shown in Figure 3.14, with different colors representing the repetitions of the voltage sweep to assess reproducibility. The devices proved to be quite stable for most of the cycles, with a noticeable hysteresis effect between the forward and backward sweeps, which is typical for OECTs due to the ionic movement within the PEDOT:PSS layer during operation[34]. The same observations made for the output characteristics apply here as well, with the device having the smallest drop spacing (80 µm) exhibiting the highest drain current (I_{DS}) values and the device with the largest drop spacing (120 µm) showing the lowest I_{DS} values. This is again consistent with the expectation that a smaller drop spacing leads to a thicker PEDOT:PSS layer, resulting in lower channel resistance and higher current flow.

The comparison between gold and silver gate is reported in Figure 3.15, which shows a more pronounced modulation of the drain current when using the silver gate (Figure 3.15b) compared to the gold gate (Figure 3.15a). This indicates that the choice of gate material can significantly influence the performance of the OECT, particularly in terms of its ability to modulate the channel current in response to changes in gate voltage. This is explained by the fact that the capacitance (per unit area) of PEDOT:PSS is generally much higher than the gate one[7]. As explained earlier, in this work the silver gate cannot be considered for biosensing applications due to biocompatibility issues, therefore this analysis is mainly for understanding the device behavior rather than for practical applications. In order to achieve better performance with gold gates, some optimization of the device geometry and fabrication process may be necessary. For instance, increasing the gate surface in contact with the electrolyte could enhance the effect of the gate voltage on the channel current[34].

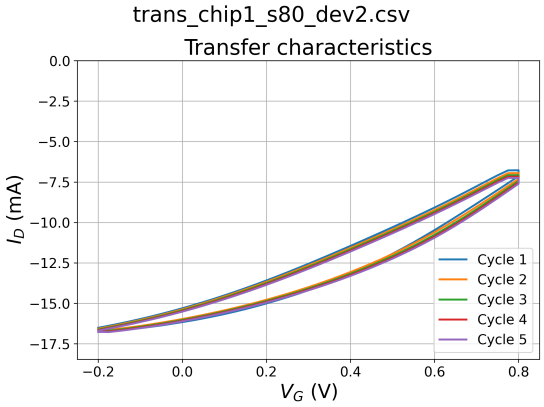

(a) Drop spacing: 80 µm

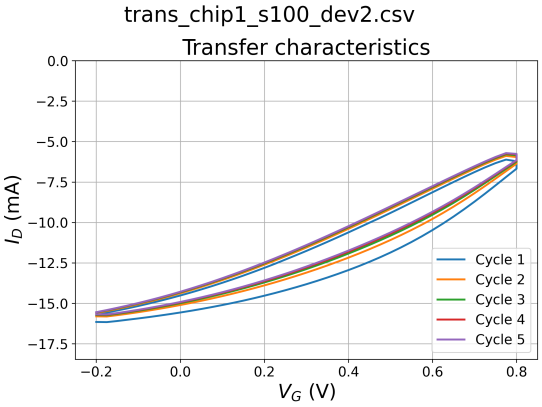

(b) Drop spacing: 100 µm

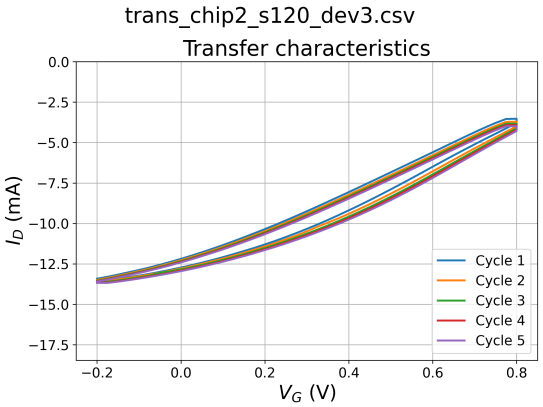

(c) Drop spacing: 120 µm

Figure 3.14: Transfer characteristics of OECTs with different drop spacings: 80 µm, 100 µm and 120 µm.

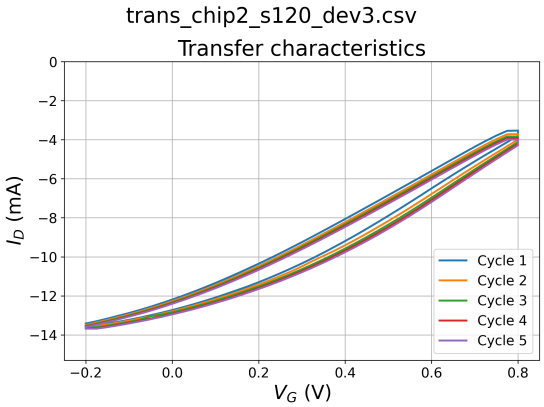

(a) With gold gate.

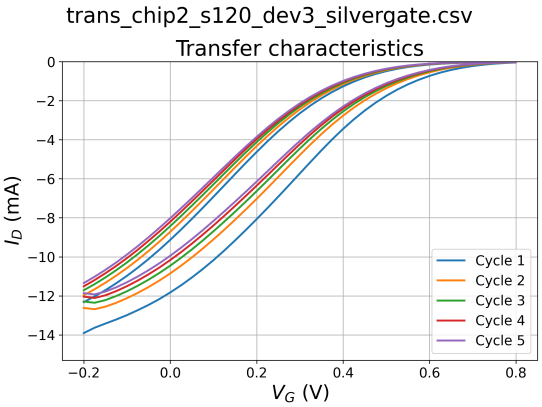

(b) With silver gate.

Figure 3.15: Comparison of transfer characteristics of OECT with 120 µm drop spacing using gold and silver gate electrodes.

Threshold Voltage Extraction

The threshold voltage V_{th} was determined using the square-root method applied to the drain current I_{DS} [5]. In the saturation regime, the current follows the quadratic relation in Equation 3.1:

$$I_{DS} \propto (V_{GS} - V_{th})^2 \tag{3.1}$$

which implies the relationship in Equation 3.2.

$$\sqrt{|I_{DS}|} \propto V_{GS} - V_{th} \tag{3.2}$$

Therefore, by plotting $\sqrt{|I_{DS}|}$ versus V_{GS} and performing a linear fit in the appropriate region, the threshold voltage is obtained as the intercept of the fitted line with the voltage axis, according to Equation 3.3, where m is the slope and q the intercept of the linear regression.

$$V_{th} = -\frac{q}{m} \tag{3.3}$$

The fitting was restricted to a gate voltage interval where the device operates in the saturation regime and the square-root relationship holds. This region was chosen to avoid the subthreshold zone and high-current deviations, typically corresponding to low V_{GS} values where the linear approximation is valid. The limits were set based on preliminary inspection of the transfer curve to ensure a high goodness of fit.

The extracted threshold voltage values for the different drop spacings and gate materials are summarized in Table 3.2. In the table both forward and backward sweeps are reported, to assess the hysteresis effects. The reported values correspond to the mean of all extracted parameters over multiple sweeps, while the associated uncertainty is expressed as the standard deviation. The results indicate that the threshold voltage decreases with increasing drop spacing, which can be attributed to the reduced channel thickness. Additionally, the device with the silver gate exhibits a significantly lower threshold voltage compared to the gold gate, confirming the improvement in performance when using silver as gate material.

Drop Spacing (µm)	Forward V_{th} (V)	Backward V_{th} (V)
80 (Au gate)	5.54 ± 0.07	3.50 ± 0.07
100 (Au gate)	4.9 ± 0.7	3.09 ± 0.08
120 (Au gate)	3.83 ± 0.17	2.61 ± 0.08
120 (Ag gate)	1.01 ± 0.09	0.67 ± 0.02

Table 3.2: Extracted threshold voltage values for different drop spacings and gate material.

Transconductance extraction

The transconductance g_m was obtained as the derivative of the drain current with respect to the gate voltage, as defined in Equation 3.4.

$$g_m = \frac{\partial I_{DS}}{\partial V_{GS}} \tag{3.4}$$

This parameter was estimated numerically by computing the discrete differences between consecutive points of I_{DS} and V_{GS} within the transfer curves. The approximation used is given by Equation 3.5.

$$g_m \approx \max\left(\frac{\Delta I_{DS}}{\Delta V_{GS}}\right) \tag{3.5}$$

The maximum value of g_m was considered as the figure of merit for each sweep direction (forward and backward). The results are summarized in Table 3.3 for different spacings and gate materials. The reported values correspond to the mean of the extracted parameters over multiple sweeps and the uncertainty was calculated as the standard deviation of g_m across repeated measurements. The transconductance is a measure of the sensitivity of the OECT to gate voltage changes, with higher values indicating better performance in modulating the channel current. The data prove that the devices with gold gate have quite similar transconductance, while the one with silver gate exhibits significantly higher values.

Drop Spacing (µm)	Forward g_m (mS)	Backward g_m (mS)
80 (Au gate)	17.6 ± 0.2	13.4 ± 0.2
100 (Au gate)	18 ± 1	12.6 ± 0.1
120 (Au gate)	14.6 ± 0.2	12.4 ± 0.1
120 (Ag gate)	22 ± 1	22.2 ± 0.7

Table 3.3: Extracted transconductance values for different drop spacings and gate material.

ON/OFF current ratio

The ON/OFF current ratio I_{ON}/I_{OFF} was calculated to evaluate the switching capability of the device. For each sweep direction, the maximum and minimum drain current values were extracted: I_{ON} corresponds to the highest current in the conductive state and I_{OFF} to the lowest current in the OFF state. The ratio was then computed using Equation 3.6.

$$\frac{I_{ON}}{I_{OFF}} = \frac{\max(|I_{DS}|)}{\min(|I_{DS}|)}. \tag{3.6}$$

The results are summarized in Table 3.4 for different drop spacings and gate materials. The reported values correspond to the mean over multiple sweeps and the variability is expressed as the standard deviation. The I_{ON}/I_{OFF} ratio is a key figure of merit for transistor performance, as it indicates the ability of the device to clearly distinguish between the ON and OFF states. A high ratio ensures low leakage current in the OFF state and strong current modulation in the ON state, which is essential for reliable switching and low-power operation. The devices with gold gate exhibit quite low ON/OFF ratios, while the one with silver gate shows a significant improvement, reaching values of order of hundreds.

The electrical measurements demonstrated that the fabricated OECTs exhibit typical transistor behavior, with the ability to modulate the drain current through gate voltage variations. The device performance was found to depend on the drop

Drop Spacing (µm)	Forward I_{ON}/I_{OFF}	Backward I_{ON}/I_{OFF}
80 (Au gate)	2.26 ± 0.06	2.36 ± 0.05
100 (Au gate)	2.50 ± 0.05	2.67 ± 0.06
120 (Au gate)	3.3 ± 0.1	3.6 ± 0.2
120 (Ag gate)	420 ± 70	700 ± 100

Table 3.4: Extracted ON/OFF current ratio for different drop spacings and gate material.

spacing used during inkjet printing, which impacts the PEDOT:PSS layer thickness and consequently the channel conductivity. The choice of gate material also plays a significant role, with silver gates providing enhanced general performances compared to gold gates. However, for biosensing applications, gold gates remain the preferred choice due to their biocompatibility and functionalization capabilities.

3.4 OECTs sensing measurements

The gates of the OECTs were functionalized with Ang-2 antibodies to enable specific binding of Ang-2 proteins as explained in Section 2.4.1, as a proof of concept for biosensing applications. These trials were executed using a microfluidic platform already validated by Segantini et al.[61] in order to ensure reliability of the experimental setup. The sensing measurements were performed by exposing the functionalized gates to PBS solutions with increasing concentrations of Ang-2 of 10, 50 and 100 pM.Figure 3.16 shows the variation of the drain current measured at fixed voltages of V_{DS} = -0.4 V and V_G = -0.2 V, after the exposure to each concentration of Ang-2. The percentage variation in current is referred to the initial current measured with pure PBS solution (0 pM Ang-2) and it was obtained according to Equation 3.7.

$$\Delta I_D = \frac{I_{D,Ang2} - I_{D,PBS}}{I_{D,PBS}} \times 100 \tag{3.7}$$

The results indicate a clear decrease in the drain current with increasing Ang-2 concentration, demonstrating the sensor capability to detect the presence of the target protein. This behavior is explained by the specific binding of Ang-2 to the immobilized antibodies on the gate surface, which affects the gate potential and therefore modulates the channel conductivity of the OECT[62].

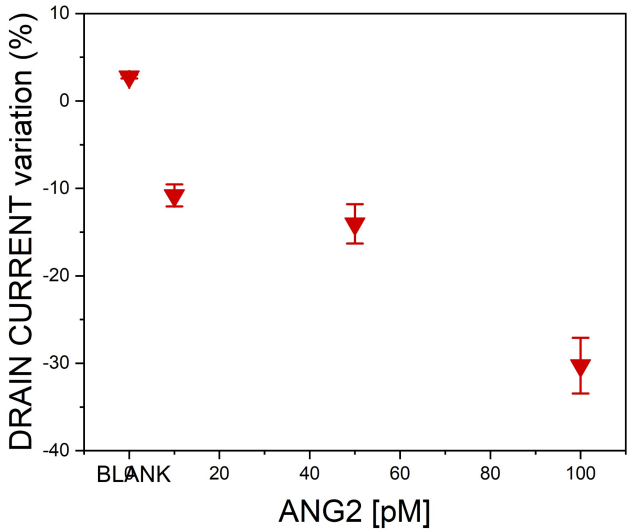

Figure 3.16: Drain current variation with Ang-2 increasing concentration.

The obtained results confirm the potential of OECTs as sensitive biosensors for the detection of specific proteins, with possible applications in medical diagnostics and biological research. Further developments of this project could focus on the choice of different biorecognition elements specific for the studied skin model and the corresponding functionalization protocols.

Chapter 4

Conclusions and Future Developments

The presented work focused on the design and fabrication of a multi-layer microfluidic platform suitable for hosting a 3D *in vitro* skin model with integrated vascular components, including OECT sensors for real-time monitoring of the tissue environment. The platform was developed to include a membrane supporting the skin model, microfluidic channels for perfusion and embedded OECTs for sensing. Two different membranes were investigated, a commercial PC membrane and a silk fibroin membrane, which required different designs. The fabrication process for the microfluidic platform consisted in replica molding of PDMS layers using 3D-printed molds, followed by adhesive or plasma bonding to assemble the layers and integrate the membrane. The sensors were fabricated separately on silicon substrates and then integrated into the platform by aligning them with dedicated openings in the PDMS layers. The electrodes of the devices were manufactured in clean room environment using standard photolithography and metal deposition techniques, then the channel was obtained by inkjet printing PEDOT:PSS.

Microfluidic leakage tests were performed on the multi-layer platforms assembles with both types of membranes and two different bonding methods (adhesive and plasma). The results demonstrated that the platforms with PC membranes exhibited good sealing and no leakage with both bonding techniques, however plasma bonding was preferred for the better uniformity and reproducibility. The platforms with silk fibroin membranes showed some limitations due to the hydrophilic nature of the membrane, which caused bending and leakages through the membrane itself.

OECTs were successfully integrated into the microfluidic platform and characterized electrically in PBS solution. The devices showed typical OECT behavior with good transconductance and stability over time, with slight variations with different inkjet parameters used for channel deposition. A proof of concept experiment was performed to demonstrate the sensing capabilities of the devices by detecting Ang2 protein through antigen-antibody binding events at the functionalized gate surface.

Future developments of this work could focus on several aspects. First, further optimization of the platform version with the silk fibroin membrane needs to be pursued to enable cell culture in this configuration. This could involve the hydrophobic treatment of the membrane to prevent bending and leakages due to absorption of fluids. The introduction of PDMS pillars in the lower part of the central chamber could also help support the membrane in case of deflection, although it would reduce the

available volume. Additionally, the microfluidic platform could be tested with the actual 3D *in vitro* skin model described by Villata et al.[23], including also vascular components, to evaluate its performance in a biological context. The OECT sensors will need to be further characterized and optimized for sensitivity and selectivity towards specific biomarkers relevant to skin physiology and pathology. Finally, long-term stability and biocompatibility studies of the entire platform would be essential to validate its suitability for extended tissue culture and monitoring applications.

Bibliography

[1] Santosh Kumar Srivastava, Guo Wei Foo, Nikhil Aggarwal, and Matthew Wook Chang. Organ-on-chip technology: Opportunities and challenges. *Biotechnology Notes*, 5:8–12, 1 2024. ISSN 2665-9069. doi:10.1016/j.biotno.2024.01.001.

[2] Min Song, Xiaogang Lin, Zhijia Peng, Shibin Xu, Lifeng Jin, Xiaodong Zheng, and Haoyue Luo. Materials and methods of biosensor interfaces with stability. *Frontiers in Materials*, 7, jan 2021. ISSN 2296-8016. doi:10.3389/fmats.2020.583739.

[3] Phirosiberia. Mosfet depletion-mode n-channel diagram. `https://commons.wikimedia.org/wiki/File:MOSFET_depletion-mode_n-channel_en.svg`, 2009. Licensed under Creative Commons Attribution-Share Alike 4.0 International.

[4] Jacob T. Friedlein, Robert R. McLeod, and Jonathan Rivnay. Device physics of organic electrochemical transistors. *Organic Electronics*, 63:398–414, 2018. ISSN 1566-1199. doi:https://doi.org/10.1016/j.orgel.2018.09.010. URL `https://www.sciencedirect.com/science/article/pii/S1566119918304683`.

[5] David Ohayon. A guide for the characterization of organic electrochemical transistors and channel materials. *Chem. Soc. Rev.*, 52:1001–1023, 2023. ISSN 1460-4744. doi:10.1039/d2cs00920j.

[6] Matteo Segantini, Alberto Ballesio, Gianluca Palmara, Pietro Zaccagnini, Francesca Frascella, Giovanna Garzone, Simone Luigi Marasso, Matteo Cocuzza, and Matteo Parmeggiani. Investigation and modeling of the electrical bias stress in electrolyte-gated organic transistors. *Advanced Electronic Materials*, 8(7), 2022. ISSN 2199-160X. doi:10.1002/aelm.202101332.

[7] Daniel A. Bernards and George G. Malliaras. Steady-state and transient behavior of organic electrochemical transistors. *Advanced Functional Materials*, 2007. doi:10.1002/adfm.200601239.

[8] Liming Bai, Cristina García Elósegui, Weiqi Li, Ping Yu, Junjie Fei, and Lanqun Mao. Biological applications of organic electrochemical transistors: Electrochemical biosensors and electrophysiology recording. *Frontiers in Chemistry*, 7, may 2019. ISSN 2296-2646. doi:10.3389/fchem.2019.00313.

[9] Namsheer K and Chandra Sekhar Rout. Conducting polymers: a comprehensive review on recent advances in synthesis, properties and applications. *RSC Advances*, 11(10):5659–5697, 2021. ISSN 2046-2069. doi:10.1039/d0ra07800j.

[10] Thanh-Hai Le, Yukyung Kim, and Hyeonseok Yoon. Electrical and electrochemical properties of conducting polymers. *Polymers*, 9(4):150, April 2017. ISSN 2073-4360. doi:10.3390/polym9040150.

[11] TyrionL. Solgel spincoating. `https://commons.wikimedia.org/wiki/File:SolGel_SpinCoating.jpg`, 2008.

[12] Saleem Khan, Shawkat Ali, and Amine Bermak. Smart manufacturing technologies for printed electronics. In Rafael Vargas-Bernal, Peng He, and Shuye Zhang, editors, *Hybrid Nanomaterials*, chapter 7. IntechOpen, 2019. doi:10.5772/intechopen.89377. URL `https://doi.org/10.5772/intechopen.89377`.

[13] MicroFab Technologies, Inc. Jetlab tabletop printing system, 2025. URL `https://www.microfab.com/products/printing-systems/jetlab-tabletop`.

[14] PiquetLab. Ink-jet printer jetlab 4. `https://piquetlab.it/ink-jet-printer-jetlab-4/`, n.d.

[15] MicroFab Technologies Inc. Optics subsystems. `https://www.microfab.com/products/optics-subsystems`, n.d.

[16] Mandeep Singh, Navpreet Kaur, and Elisabetta Comini. The role of self-assembled monolayers in electronic devices. *Journal of Materials Chemistry C*, 8(12):3938–3955, 2020. ISSN 2050-7526. doi:10.1039/d0tc00388c.

[17] Harvard Apparatus. *Model 33 Twin Syringe Pump User's Manual*. Holliston, MA, USA, 2012. URL `https://www.harvardapparatus.com/media/harvard/pdf/Model_33_Users_Manual.pdf`. Publication No. 5390-001, Revision B.

[18] Keysight Technologies. B2912a precision source/measure unit, 2 ch, 10 fa, 210 v, 3 a dc/10.5 a pulse, 2021. URL `https://www.keysight.com/us/en/product/B2912A/precision-source-measure-unit-2-ch-10fa-210v-3a-dc-10-5a-pulse.html`.

[19] Oxyphen AG. Unique-mem® track-etched membranes, n.d. URL `https://www.oxyphen.com/technologies/unique-mem-unlaminated-track-etched-membranes/`.

[20] Fondazione D^{3}4Health. Home — fondazione d^{3}4health. `https://d34health.it/`, 2025.

[21] Politecnico di Torino. Ecosistema d34health, il politecnico finanzia nuove ricerche per l'innovazione in ambito sanitario e assistenziale. `https://www.polito.it/ateneo/comunicazione-e-ufficio-stampa/poliflash/ecosistema-d34health-il-politecnico-finanzia-nuove-ricerche`, 2025.

[22] Mohammad Imran, Peter Michael Moyle, Danielle Kamato, and Yousuf Mohammed. Advances in, and prospects of, 3d preclinical models for skin drug discovery. *Drug Discovery Today*, 29(12):104208, 2024. ISSN 1359-6446. doi:10.1016/j.drudis.2024.104208.

[23] Simona Villata, Désirée Baruffaldi, Raquel Cue Lopez, Camilla Paoletti, Paula Bosch, Lucia Napione, Andrea M. Giovannozzi, Candido Fabrizio Pirri, Enrique Martinez-Campos, and Francesca Frascella. Broadly accessible 3d in vitro skin model as a comprehensive platform for antibacterial therapy screening. *ACS Applied Materials & Interfaces*, 16(51):70284–70296, 2024. doi:10.1021/acsami.4c16397. URL `https://doi.org/10.1021/acsami.4c16397`. PMID: 39667725.

[24] Shagun Gupta, Kritika Ramesh, Suhaib Ahmed, and Vipan Kakkar. Lab-on-chip technology: A review on design trends and future scope in biomedical applications. *International Journal of Bio-Science and Bio-Technology*, 8:311–322, 10 2016. doi:10.14257/ijbsbt.2016.8.5.28.

[25] Licciardello M., Traldi C., Cicolini M., Bertana V., Marasso S.L., Cocuzza M., Tonda-Turo C., and Ciardelli G. A miniaturized multicellular platform to mimic the 3d structure of the alveolar-capillary barrier. *Frontiers in Bioengineering and Biotechnology*, 12, 2024. ISSN 2296-4185. doi:10.3389/fbioe.2024.1346660.

[26] Peng Lin and Feng Yan. Organic thin-film transistors for chemical and biological sensing. *Advanced Materials*, 24:34–51, 2012. doi:10.1002/adma.201103334.

[27] Deepa Chaturvedi, Swarali Paranjape, Ratnesh Jain, and Prajakta Dandekar. Disease-related biomarkers as experimental endpoints in 3d skin culture models. *Cytotechnology*, 75(3):165–193, April 2023. ISSN 1573-0778. doi:10.1007/s10616-023-00574-2.

[28] Isabella J. Tan, Alicia Podwojniak, Aarushi Parikh, and Bernard A. Cohen. Precision dermatology: A review of molecular biomarkers and personalized therapies. *Current Issues in Molecular Biology*, 46(4):2975–2990, March 2024. ISSN 1467-3045. doi:10.3390/cimb46040186.

[29] A. T. Giannitsis and M. Min. Usage of microfluidic lab-on-chips in biomedicine. In *2010 12th Biennial Baltic Electronics Conference*, pages 249–252, 2010. doi:10.1109/BEC.2010.5630239.

[30] Subhashinee Singh, Nabanita Das, Manisha Rathore, Ambresh Nishad, Nisha Kumari, and Rajdeep Guha. Organ-on-a-chip (ooac) technology: Impact on drug screening and personalized medicine. *Regenerative Engineering and Translational Medicine*, April 2025. ISSN 2364-4141. doi:10.1007/s40883-025-00409-w.

[31] Bing Li, Yuanjun Tang, Zhanya Huang, Lijun Ma, Jiagui Song, and Lixiang Xue. Synergistic innovation in organ-on-a-chip and organoid technologies: reshaping the future of disease modeling, drug development, and precision medicine. *Protein & Cell*, jul 2025. ISSN 1674-8018. doi:10.1093/procel/pwaf058.

[32] Sangeeta N Bhatia and Donald E Ingber. Microfluidic organs-on-chips. *Nature Biotechnology*, 32(8):760–772, August 2014. ISSN 1546-1696. doi:10.1038/nbt.2989.

[33] Manuel Saldana, Sandra Gallegos, Edelmira Gálvez, Jonathan Castillo, Eleazar Salinas-Rodríguez, Eduardo Cerecedo-Sáenz, Juan Hernández-Ávila, Alessandro Navarra, and Norman Toro. The reynolds number: A journey from its origin to modern applications. *Fluids*, 9(12), 2024. ISSN 2311-5521. doi:10.3390/fluids9120299. URL `https://www.mdpi.com/2311-5521/9/12/299`.

[34] Jonathan Rivnay, Sahika Inal, Alberto Salleo, Róisín M. Owens, Magnus Berggren, and George G. Malliaras. Organic electrochemical transistors. *Nature Reviews Materials*, 3(2), January 2018. ISSN 2058-8437. doi:10.1038/natrevmats.2017.86.

[35] Jovana Babic, Alberto Ballesio, Francesca Frascella, Lucia Napione, Mattia Pagani, Matteo Parmeggiani, and Simone Luigi Marasso. A contamination-free electrolyte-gated organic transistors platform for high-accuracy tumor biomarker detection. *Sensors and Actuators Reports*, 9:100341, June 2025. ISSN 2666-0539. doi:10.1016/j.snr.2025.100341.

[36] Giovanni Ghione. *Dispositivi per la microelettronica*. McGraw-Hill Education, 2003. ISBN 9788838607684.

[37] Yue Niu, Ze Qin, Ying Zhang, Chao Chen, Sha Liu, and Hu Chen. Expanding the potential of biosensors: a review on organic field effect transistor (ofet) and organic electrochemical transistor (oect) biosensors. *Materials Futures*, 2(4): 042401, aug 2023. ISSN 2752-5724. doi:10.1088/2752-5724/ace3dd.

[38] Maria H. Bolin, Karl Svennersten, David Nilsson, Anurak Sawatdee, Edwin W. H. Jager, Agneta Richter-Dahlfors, and Magnus Berggren. Active control of epithelial cell density gradients grown along the channel of an organic electrochemical transistor. *Advanced Materials*, 21(43):4379–4382, nov 2009. ISSN 1521-4095. doi:10.1002/adma.200901191.

[39] Y. Roichman, Y. Preezant, and N. Tessler. Analysis and modeling of organic devices. *physica status solidi (a)*, 201(6):1246–1262, May 2004. ISSN 1521-396X. doi:10.1002/pssa.200404342.

[40] Peng Lin, Feng Yan, Jinjiang Yu, Helen L. W. Chan, and Mo Yang. The application of organic electrochemical transistorsin cell-based biosensors. *Advanced Materials*, 22:3655–3660, 2010. doi:10.1002/adma.201000971.

[41] Piquet (piemonte quantum enabling technology), 2023. URL `https://www.polito.it/ricerca/luoghi/infrastrutture-di-ricerca/piquet`.

[42] Politobiomed lab, 2025. URL `https://www.polito.it/ricerca/luoghi/centri-interdipartimentali/politobiomed-lab`.

[43] Robert McNeel & Associates. *Rhinoceros 3D, Version 8*. Robert McNeel & Associates, Seattle, WA, USA, 2023. URL `https://www.rhino3d.com/`.

[44] KLISBio S.r.l. Why silk. `https://www.klis.bio/why_silk`, n.d.

[45] Stratasys. J35™ pro 3d printer. `https://www.stratasys.com/en/3d-printers/printer-catalog/polyjet/j35-pro-printer/`, n.d..

[46] Stratasys. Guide to 3d printing: Polyjet technology. https://www.stratasys.com/en/guide-to-3d-printing/technologies-and-materials/polyjet-technology/, n.d..

[47] N. Muthuram, P. Sriram Madhav, D. Keerthi Vasan, Manav Eshwar Mohan, and G. Prajeeth. A review of recent literatures in poly jet printing process. *Materials Today: Proceedings*, 68:1906–1920, 8 2022. ISSN 2214-7853. doi:10.1016/j.matpr.2022.08.090.

[48] Jackson Sanders, Xingjian Wei, and Zhijian Pei. Experimental investigation of polyjet 3d printing: Effects of sample location and volume on power consumption. *Manufacturing Letters*, 31:83–86, January 2022. ISSN 2213-8463. doi:10.1016/j.mfglet.2021.07.013.

[49] Stratasys. Veroultrawhite material specification. https://www.stratasys.com/en/materials/materials-catalog/polyjet-materials/veroultra/, n.d..

[50] Stratasys. Veroultraclear material specification. https://www.stratasys.com/en/materials/materials-catalog/polyjet-materials/veroultraclear/, n.d..

[51] Bastien Venzac, Shanliang Deng, Ziad Mahmoud, Aufried Lenferink, Aurélie Costa, Fabrice Bray, Cees Otto, Christian Rolando, and Séverine Le Gac. Pdms curing inhibition on 3d-printed molds: Why? also, how to avoid it? *Analytical Chemistry*, 93(19):7180–7187, 2021. ISSN 0003-2700. doi:10.1021/acs.analchem.0c04944.

[52] Rui A. Lima. The impact of polydimethylsiloxane (pdms) in engineering: Recent advances and applications. *Fluids*, 10(2):41, February 2025. ISSN 2311-5521. doi:10.3390/fluids10020041.

[53] Inês Miranda, Andrews Souza, Paulo Sousa, João Ribeiro, Elisabete M. S. Castanheira, Rui Lima, and Graça Minas. Properties and applications of pdms for biomedical engineering: A review. *Journal of Functional Biomaterials*, 13 (1):2, December 2021. ISSN 2079-4983. doi:10.3390/jfb13010002.

[54] Alvaro Mata, Aaron Fleischman, and Shuvo Roy. Characterization of polydimethylsiloxane (pdms) properties for biomedical micro/nanosystems. *Biomedical Microdevices*, 7(4):281–293, 2005. ISSN 1572-8781. doi:10.1007/s10544-005-6070-2.

[55] The Dow Chemical Company. *SYLGARD 184 Silicone Elastomer*, n.d.

[56] MicroChemicals GmbH. *AZ 5214E Image Reversal Photoresist*, 2009. URL http://dvh.physics.illinois.edu/pdf/AZ5214E.pdf. Product datasheet for AZ 5214E photoresist.

[57] Giorgia Rinaldi, Davide Vurro, Martina Cicolini, Jovana Babic, Aris Liboà, Giuseppe Tarabella, Pasquale D'Angelo, Simone L. Marasso, Matteo Cocuzza,

Lorenzo Vigna, Fabrizio C. Pirri, and Matteo Parmeggiani. Pedot:pss deposition in oects: Inkjet printing, aerosol jet printing and spin coating. *Micro and Nano Engineering*, 24:100272, September 2024. ISSN 2590-0072. doi:10.1016/j.mne.2024.100272.

[58] Quentin Thiburce, Nicholas Melosh, and Alberto Salleo. Wafer-scale microfabrication of flexible organic electrochemical transistors. *Flexible and Printed Electronics*, 7(3):034001, July 2022. ISSN 2058-8585. doi:10.1088/2058-8585/ac808a.

[59] L. Jay Deiner and Thomas L. Reitz. Inkjet and aerosol jet printing of electrochemical devices for energy conversion and storage. *Advanced Engineering Materials*, 19(7), March 2017. ISSN 1527-2648. doi:10.1002/adem.201600878.

[60] Heraeus Epurio. Clevios™ ph 1000 product datasheet. `https://www.heraeus-epurio.com/dam/jcr:27ca5b86-9b86-4fac-be12-6d857b77f694/clevios-ph-1000.pdf`, n.d.

[61] Matteo Segantini, Matteo Parmeggiani, Alberto Ballesio, Gianluca Palmara, Francesca Frascella, Simone Luigi Marasso, and Matteo Cocuzza. Design of a portable microfluidic platform for egot-based in liquid biosensing. *Sensors*, 22 (3):969, 2022. doi:10.3390/S22030969.

[62] Denjung Wang, Vincent Noël, and Benoît Piro. Electrolytic gated organic field-effect transistors for application in biosensors—a review. *Electronics*, 5 (1):9, February 2016. ISSN 2079-9292. doi:10.3390/electronics5010009.

Appendix I

Supplementary data and figures

Here are reported the characteristics of all the fabricated OECTs, not included in the main text. Each figure shows the output and transfer characteristics of the device. The extracted parameters for all the devices are summarized in Table 4.1. Note that the device number 1 of the chip with 100 µm drop spacing presented a much lower current compared to the other two devices on the same chip, probably due to a fabrication defect; for this reason, its parameters are quite different from the others.

			V_{th} (V)	g_m (mS)	I_{ON}/I_{OFF}
Spacing: 80 µm Au gate	Dev1	Forward	5.1 ± 0.2	13.0 ± 0.3	2.18 ± 0.07
		Backward	3.19 ± 0.07	9.1 ± 0.3	2.30 ± 0.07
	Dev2	Forward	5.54 ± 0.07	17.6 ± 0.3	2.26 ± 0.06
		Backward	3.50 ± 0.07	13.4 ± 0.2	2.36 ± 0.05
	Dev3	Forward	7 ± 1	17 ± 2	1.79 ± 0.02
		Backward	4.4 ± 0.1	10.29 ± 0.03	1.87 ± 0.03
Spacing: 100 µm Au gate	Dev1	Forward	2.1 ± 0.2	4.18 ± 0.07	8.1 ± 0.7
		Backward	1.53 ± 0.06	3.99 ± 0.01	8.9 ± 0.8
	Dev2	Forward	4.9 ± 0.7	18 ± 1	2.50 ± 0.05
		Backward	3.09 ± 0.09	12.6 ± 0.1	2.67 ± 0.06
	Dev3	Forward	5.4 ± 0.3	16.7 ± 0.7	2.24 ± 0.01
		Backward	3.56 ± 0.05	11.67 ± 0.03	2.37 ± 0.02
Spacing: 120 µm Au gate	Dev1	Forward	4.1 ± 0.2	14.3 ± 0.6	3.05 ± 0.02
		Backward	2.58 ± 0.01	11.05 ± 0.06	3.29 ± 0.01
	Dev2	Forward	4.2 ± 0.3	16.6 ± 0.9	2.91 ± 0.01
		Backward	2.68 ± 0.02	12.76 ± 0.07	3.11 ± 0.02
	Dev3	Forward	3.8 ± 0.2	14.6 ± 0.2	3.3 ± 0.1
		Backward	2.61 ± 0.08	12.45 ± 0.06	3.6 ± 0.2
Spacing: 120 µm Ag gate	Dev1	Forward	0.85 ± 0.05	20 ± 1	780 ± 70
		Backward	0.57 ± 0.01	19.8 ± 0.7	1160 ± 80
	Dev2	Forward	0.97 ± 0.07	23.3 ± 0.8	410 ± 70
		Backward	0.65 ± 0.01	23.7 ± 0.5	670 ± 90
	Dev3	Forward	1.01 ± 0.09	22 ± 1	420 ± 70
		Backward	0.67 ± 0.02	22.2 ± 0.7	700 ± 100

Table 4.1: Extracted parameters (mean ± standard deviation) for forward and backward sweeps of three devices.

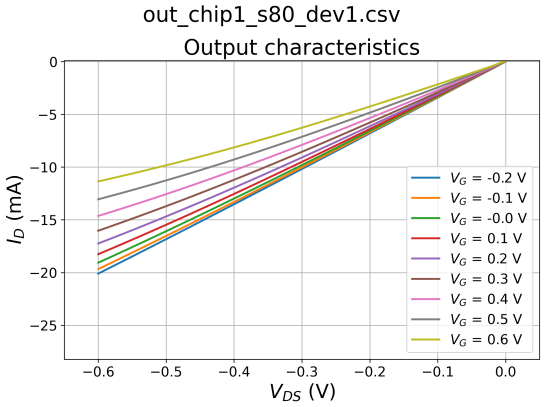

(a) Output curve for Device 1.

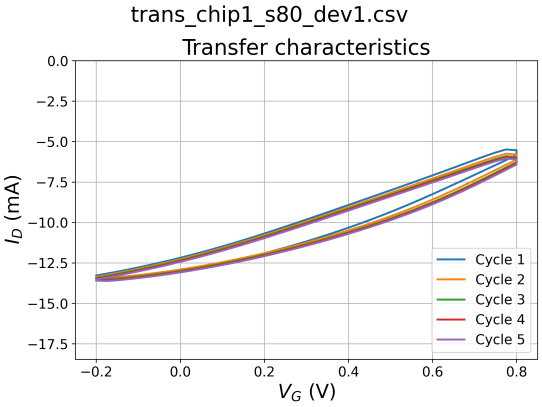

(b) Transfer curve for Device 1.

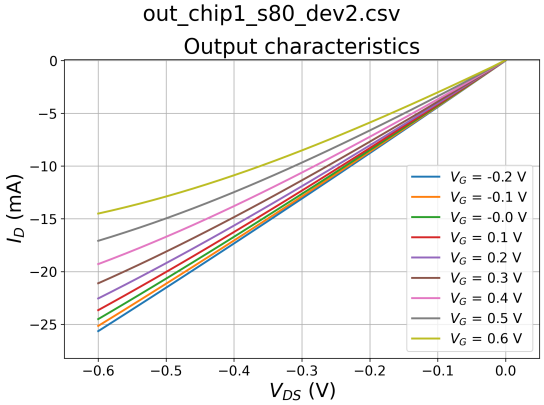

(c) Output curve for Device 2.

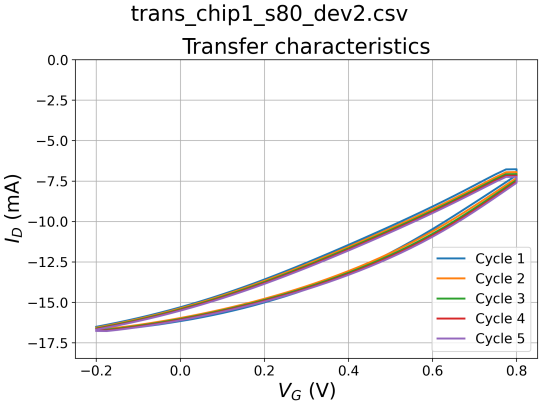

(d) Transfer curve for Device 2.

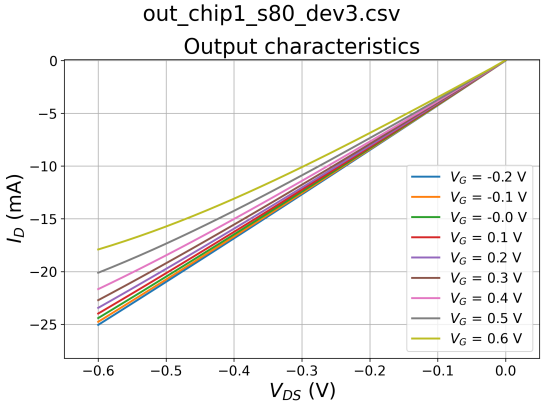

(e) Output curve for Device 3.

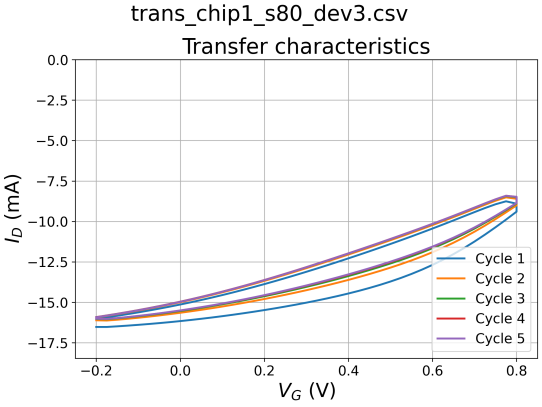

(f) Transfer curve for Device 3.

Figure 4.1: Output and transfer characteristics of OECTs with 80 µm inkjet drop spacing and Au gate.

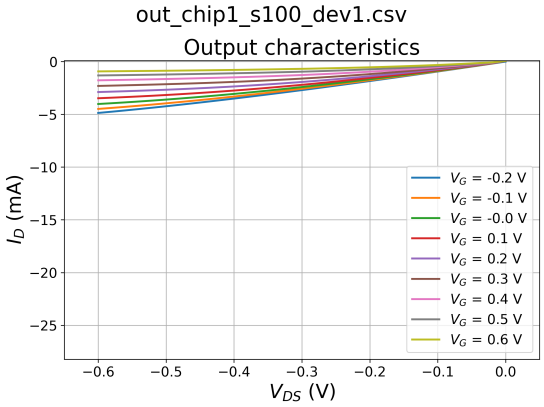

(a) Output curve for Device 1.

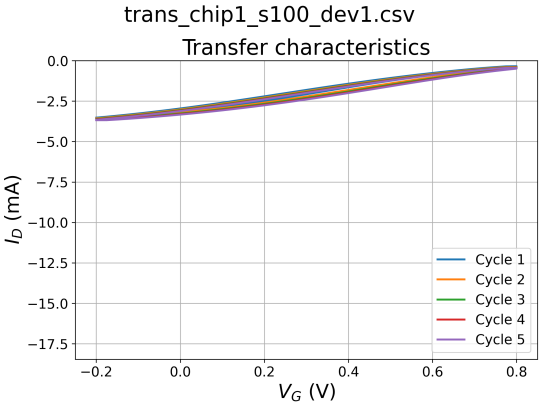

(b) Transfer curve for Device 1.

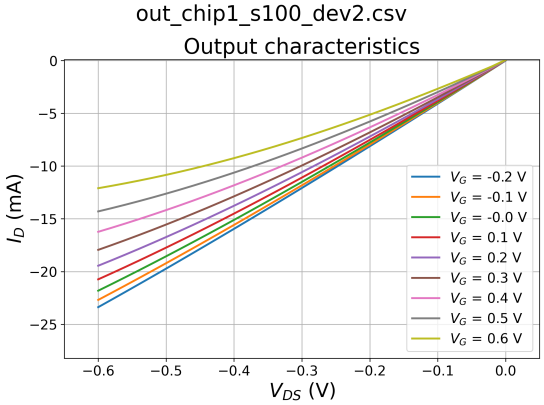

(c) Output curve for Device 2.

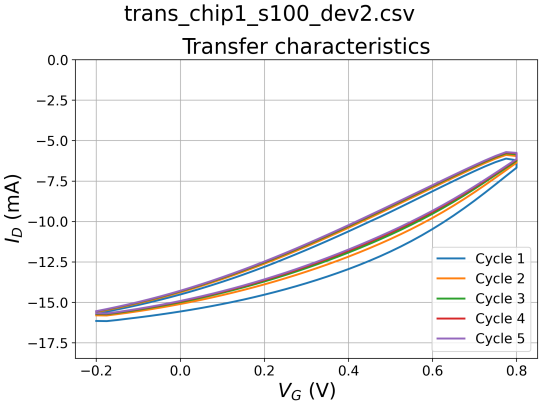

(d) Transfer curve for Device 2.

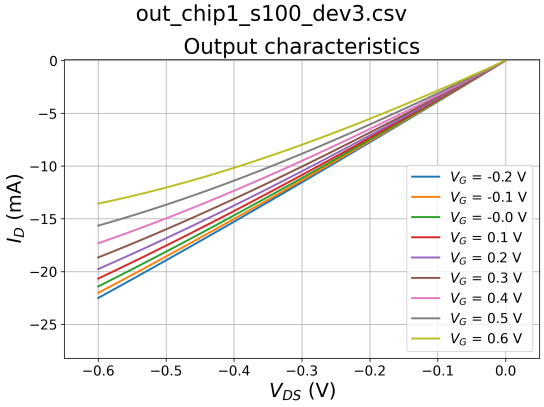

(e) Output curve for Device 3.

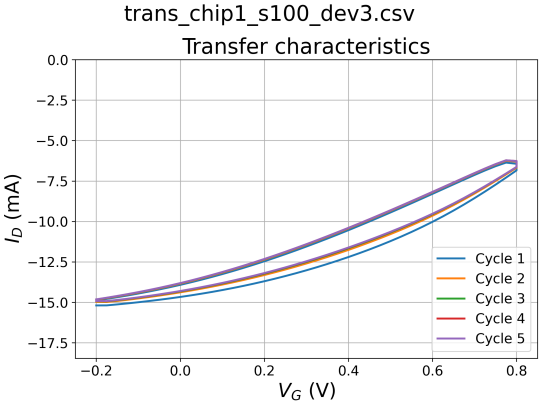

(f) Transfer curve for Device 3.

Figure 4.2: Output and transfer characteristics of OECTs with 100 µm inkjet drop spacing and Au gate.

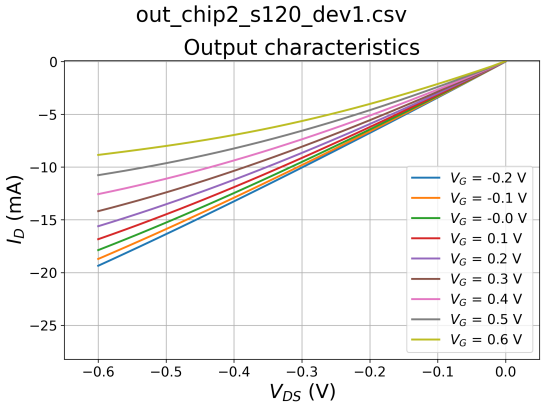

(a) Output curve for Device 1.

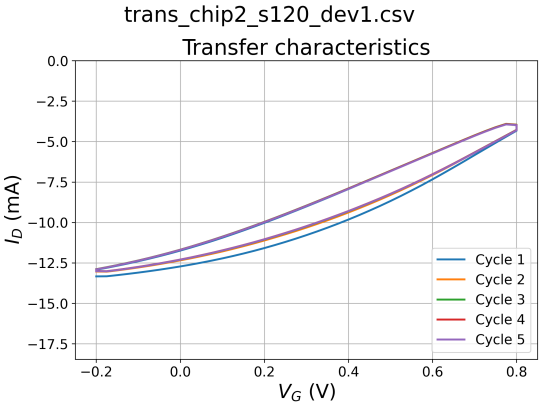

(b) Transfer curve for Device 1.

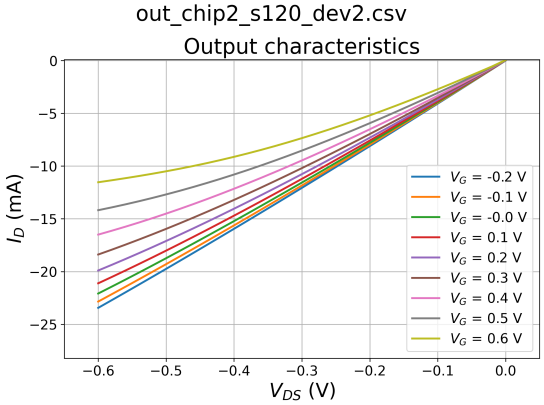

(c) Output curve for Device 2.

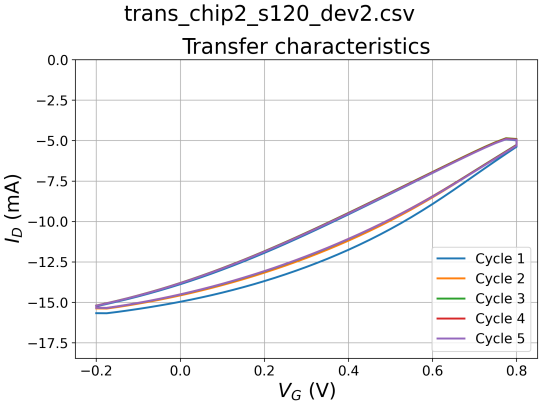

(d) Transfer curve for Device 2.

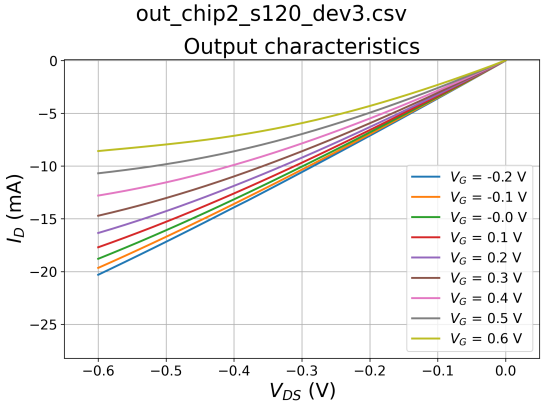

(e) Output curve for Device 3.

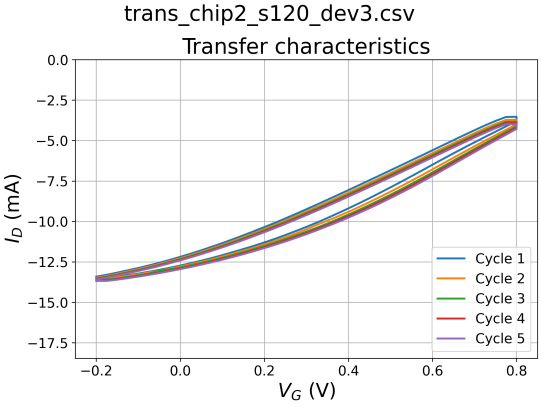

(f) Transfer curve for Device 3.

Figure 4.3: Output and transfer characteristics of OECTs with 120 µm inkjet drop spacing and Au gate.

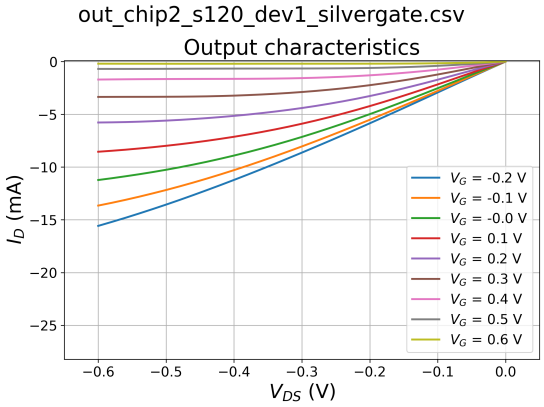

(a) Output curve for Device 1.

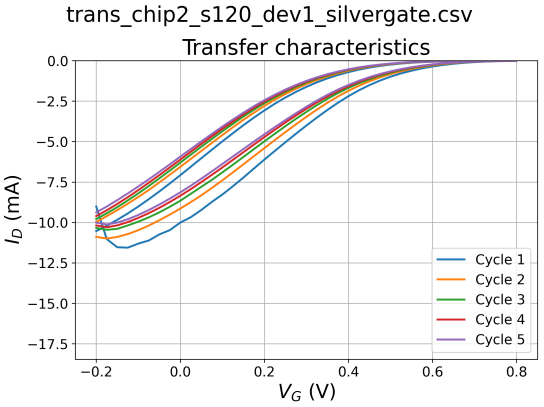

(b) Transfer curve for Device 1.

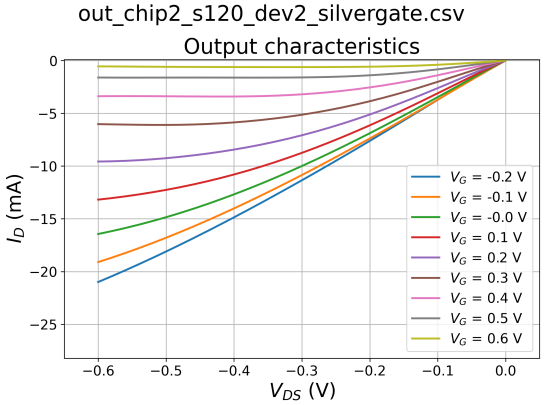

(c) Output curve for Device 2.

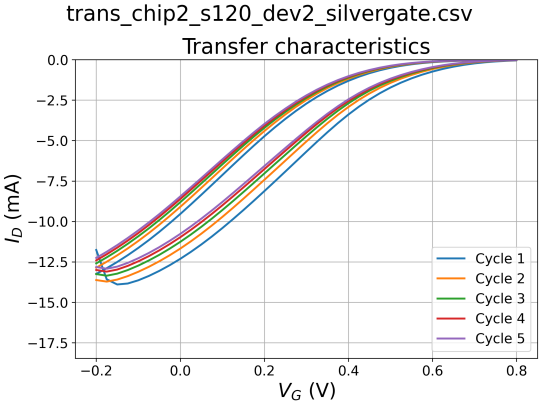

(d) Transfer curve for Device 2.

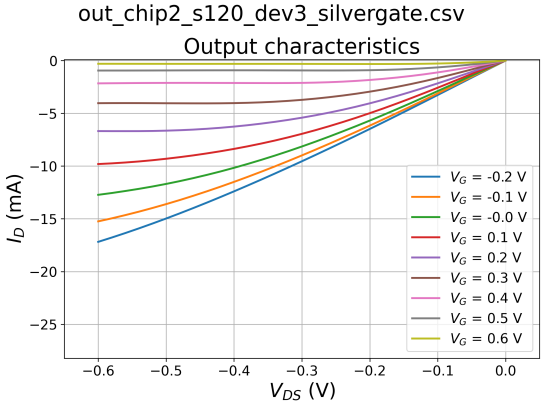

(e) Output curve for Device 3.

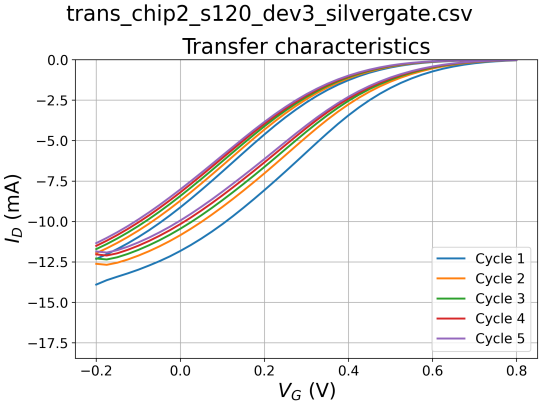

(f) Transfer curve for Device 3.

Figure 4.4: Output and transfer characteristics of OECTs with 120 µm inkjet drop spacing and Ag gate.